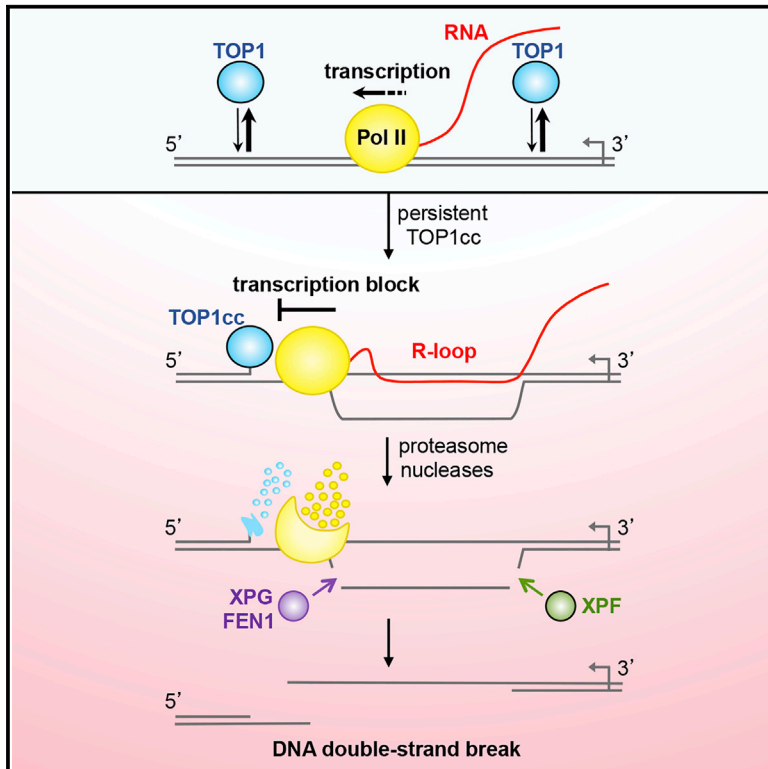# Dual Processing of R-Loops and Topoisomerase I Induces Transcription-Dependent DNA Double-Strand Breaks

Graphical Abstract

Authors

Agnese Cristini, Giulia Ricci, Sébastien Britton, ..., Giovanni Capranico, Natalia Gromak, Olivier Sordet

Correspondence

natalia.gromak@path.ox.ac.uk (N.G.), olivier.sordet@inserm.fr (O.S.)

In Brief

Cristini et al. identify a mechanism of DSB formation in non-replicating cells, which strictly depends on transcription. They are formed by two single-strand breaks on opposing DNA strands resulting from the processing of both R-loops and topoisomerase I, and genetic defects increasing these transcriptional DSBs cause neurological disorders.

Highlights

- Persistent TOP1ccs induce transcription block and R-loop formation

- Removal of transcription-blocking TOP1ccs by the TDP1 pathway generates SSBs

- Dual incision of R-loops by the nucleases XPF, XPG, and FEN1 generates SSBs

- Transcriptional DSBs are formed by these two nearby SSBs on opposing DNA strands

CellPress

Article

Dual Processing of R-Loops and Topoisomerase I Induces Transcription-Dependent DNA Double-Strand Breaks

Agnese Cristini,[1,2] Giulia Ricci,[1,3] Sébastien Britton,[4] Simona Salimbeni,[1,3] Shar-yin Naomi Huang,[5] Jessica Marinello,[3] Patrick Calsou,[4] Yves Pommier,[5] Gilles Favre,[1] Giovanni Capranico,[3] Natalia Gromak,[2,*] and Olivier Sordet[1,6,*]

[1]Cancer Research Center of Toulouse, INSERM, Université de Toulouse, Université Toulouse III Paul Sabatier, CNRS, 31037 Toulouse, France
[2]Sir William Dunn School of Pathology, University of Oxford, South Parks Road, Oxford OX1 3RE, UK
[3]Department of Pharmacy and Biotechnology, University of Bologna, 40126 Bologna, Italy
[4]Institut de Pharmacologie et Biologie Structurale, IPBS, Université de Toulouse, CNRS, UPS, Equipe Labellisée Ligue contre le Cancer 2018, 31077 Toulouse, France
[5]Developmental Therapeutics Branch and Laboratory of Molecular Pharmacology, Center for Cancer Research, National Cancer Institute, NIH, Bethesda, MD, USA
[6]Lead Contact
*Correspondence: natalia.gromak@path.ox.ac.uk (N.G.), olivier.sordet@inserm.fr (O.S.)
https://doi.org/10.1016/j.celrep.2019.08.041

SUMMARY

Although accumulation of DNA damage and genomic instability in resting cells can cause neurodegenerative disorders, our understanding of how transcription produces DNA double-strand breaks (DSBs) is limited. Transcription-blocking topoisomerase I cleavage complexes (TOP1ccs) are frequent events that prime DSB production in non-replicating cells. Here, we report a mechanism of their formation by showing that they arise from two nearby single-strand breaks (SSBs) on opposing DNA strands: one SSB from the removal of transcription-blocking TOP1ccs by the TDP1 pathway and the other from the cleavage of R-loops by endonucleases, including XPF, XPG, and FEN1. Genetic defects in TOP1cc removal (TDP1, PNKP, and XRCC1) or in the resolution of R-loops (SETX) enhance DSB formation and prevent their repair. Such deficiencies cause neurological disorders. Owing to the high frequency of TOP1cc trapping and the widespread distribution of R-loops, these persistent transcriptional DSBs could accumulate over time in neuronal cells, contributing to the neurodegenerative diseases.

INTRODUCTION

In metazoans, most cells are slow- or non-replicating, and the accumulation of DNA damage and genomic instability in such cells can cause several human diseases, including neurodegenerative syndromes (McKinnon, 2017; Rass et al., 2007). Even so, exactly how DNA double-strand breaks (DSBs), the most harmful genomic lesions, are generated in resting cells is unclear. Increasing evidence indicates that transcription can induce DNA damage and genomic instability, particularly through R-loop structures (Aguilera and García-Muse, 2012; Aguilera and Gómez-González, 2017; Sollier and Cimprich, 2015). Furthermore, co-transcriptional R-loops have been associated with neurodegenerative diseases (Groh and Gromak, 2014). R-loops consist of a RNA/DNA hybrid and a displaced single-strand DNA, formed by the reannealing of the nascent transcript with the transcribed DNA strand behind the elongating RNA polymerase II (Pol II). R-loops are widespread dynamic structures (Sanz et al., 2016). They occur naturally during transcription and have important physiological functions, such as gene expression, DNA replication, and repair (Santos-Pereira and Aguilera, 2015; Skourti-Stathaki and Proudfoot, 2014; Sollier and Cimprich, 2015). Several factors regulate R-loop homeostasis and so prevent the accumulation of unscheduled R-loops and DNA damage, including topoisomerase I (TOP1) (Drolet et al., 2003; El Hage et al., 2010; Manzo et al., 2018) and mRNA processing factors (Huertas and Aguilera, 2003; Li and Manley, 2005). Once formed, R-loops can be removed by RNase H enzymes, which degrade the RNA in the RNA/DNA hybrids (Cerritelli and Crouch, 2009), and by RNA/DNA helicases, such as senataxin (SETX) (Groh et al., 2017; Skourti-Stathaki et al., 2011), aquarius (AQR) (Sollier et al., 2014), and DHX9 (Cristini et al., 2018), which unwind the RNA/DNA hybrids.

Deregulation of TOP1 activity is a source of transcription-associated genomic instability, also associated with neurodegenerative disorders (Jiang et al., 2017; Katyal et al., 2014; Pommier et al., 2016; Takashima et al., 2002). TOP1 solves DNA topological problems arising during transcription. It relaxes both positive and negative DNA supercoiling generated ahead and behind the elongating Pol II, respectively, by forming transient TOP1 cleavage complexes (TOP1ccs), which are TOP1-linked single-strand breaks (SSBs) (Pommier et al., 2016). After DNA relaxation, TOP1ccs reverse rapidly and TOP1 is released. These transient TOP1ccs are readily stabilized or "trapped" on chromatin under physiological or pathological conditions, giving rise to irreversible TOP1ccs. DNA alterations, including oxidative lesions, base mismatches, modifications and losses, and DNA

breaks, can trap TOP1ccs (Huang et al., 2017; Pommier et al., 2016). Genetic defects in TDP1, ATM, and XRCC1 proteins cause neurological disorders and result in long-lived TOP1ccs (Hoch et al., 2017; Jiang et al., 2017; Katyal et al., 2014; Pommier et al., 2016; Takashima et al., 2002). TOP1ccs are selectively trapped by camptothecin (CPT) and its derivatives used as anti-cancer agents (Pommier, 2006).

Trapped TOP1ccs are potent transcription-blocking DNA lesions (Capranico et al., 2007; Pommier, 2006), and their repair depends primarily on the TDP1 excision pathway (Cristini et al., 2016; El-Khamisy et al., 2005; Miao et al., 2006; Yang et al., 1996). Although TOP1 depletion increases R-loop levels (Drolet et al., 2003; El Hage et al., 2010; Manzo et al., 2018; Tuduri et al., 2009), the effect of TOP1cc trapping on R-loops is less well understood except for specific genes, including snord116 (Powell et al., 2013), frataxin in Friedreich ataxia cells (Groh et al., 2014), and β-actin (Cristini et al., 2018), where R-loops are increased in response to CPT and/or derivatives. A consequence of transcription blocking by TOP1ccs is the production of DSBs, which have been detected in non-replicating cells, such as post-mitotic neurons (Sordet et al., 2009) and quiescent fibroblasts (Cristini et al., 2016). Here, we describe how these DSBs are produced and so provide a molecular mechanism that strictly depends on transcription. We show that these DSBs can arise from two nearby SSBs on opposing DNA strands, both produced during transcription: one SSB results from removal of a transcription-blocking TOP1cc by the TDP1 pathway and the other from cleavage of an R-loop by structure-specific endonucleases. Notably, genetic defects in the transcription-blocking TOP1cc removal pathway or in the resolution of R-loops enhance DSB levels by increasing their production and preventing their repair and lead to cell death. Such defects may underlie neurological diseases. Given the frequency of TOP1ccs and the widespread distribution of R-loops, these persistent transcriptional DSBs will accumulate over time in neuronal cells and so contribute to neurodegenerative diseases.

RESULTS

Transcriptional DSBs Depend on SSB Intermediates Produced during TOP1cc Removal

To investigate how DSBs are produced in response to transcription-blocking TOP1ccs, we induced these breaks by exposing quiescent WI38 hTERT fibroblasts to CPT (Cristini et al., 2016). CPT induces high levels of stabilized TOP1ccs (Pommier, 2006). Quiescence was controlled by the lack of 5-ethynyl-2'-deoxyuridine (EdU) incorporation into DNA (Figures S1A and S1B) as reported (Cristini et al., 2016). These transcriptional DSBs can be visualized by microscopy as nuclear foci containing γH2AX (phosphorylated H2AX at S139) and p53BP1 (phosphorylated 53BP1 at S1778; Figures 1A and 1B) and by neutral comet assays as increased comet tail moment (Figures 1C and 1D).

We previously showed that TOP1 degradation by the ubiquitin-proteasome pathway is required for the production of transcriptional DSBs in CPT-treated quiescent cells (Cristini et al., 2016). TOP1 degradation primes the repair of transcription-blocking TOP1ccs, giving rise to a DNA single-strand break (SSB) intermediate, which is successively processed by TDP1
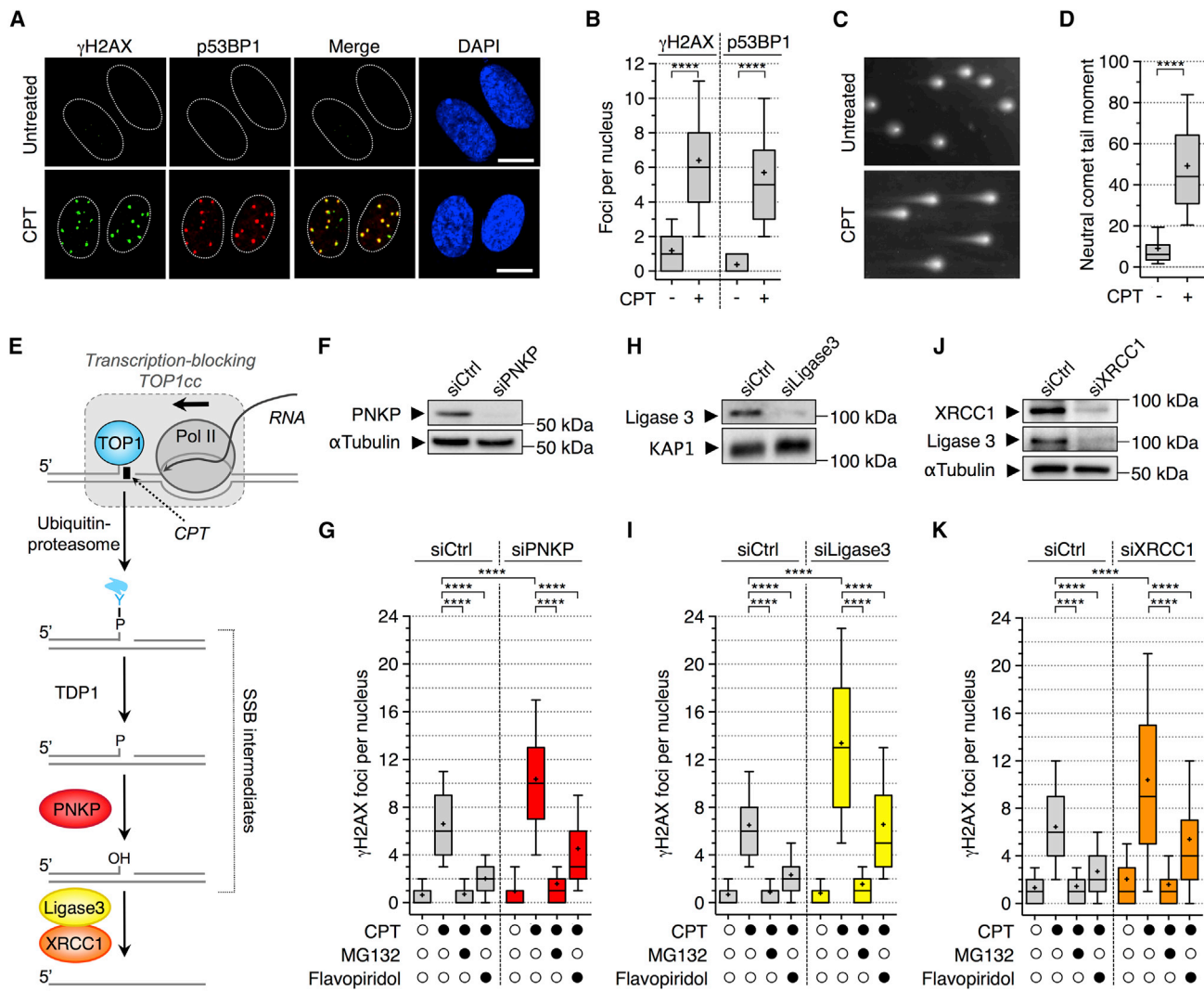
and PNKP at the 3' end before DNA re-ligation by the DNA ligase 3-XRCC1 complex (Figure 1E). Here, we asked whether these SSB intermediates contribute to the formation of transcriptional DSBs.

We also reported that TDP1-depleted cells, which accumulate TOP1 peptide-linked SSB intermediates (Figure 1E; El-Khamisy et al., 2005; Interthal et al., 2005; Miao et al., 2006), accumulate transcriptional DSBs in response to CPT (Cristini et al., 2016). To further examine the role of SSB intermediates, we depleted PNKP and the DNA ligase 3-XRCC1 complex to accumulate cellular SSBs with 3'-P and 3'-OH, respectively (Figure 1E; Ashour et al., 2015; Pommier et al., 2014). RNAi-mediated knockdown of PNKP and DNA ligase 3 in quiescent cells increased the number of γH2AX and p53BP1 foci in response to CPT (Figures 1F–1I, S1C, and S1D), which correlated with increased SSBs in alkaline comet assays (Figures S1F and S1G). Inhibition of TOP1 degradation with the proteasome inhibitor MG132, which prevented the generation of these SSB intermediates (Ashour et al., 2015; Pommier et al., 2014), suppressed the induction of γH2AX foci by CPT upon depletion of PNKP and DNA ligase 3 (Figures 1G and 1I). Under these conditions, p53BP1 foci could not be assessed because MG132 prevents the ubiquitin-dependent accumulation of 53BP1 at DSB sites (Mailand et al., 2007). The transcriptional origin of these DSB-associated foci was established by the use of flavopiridol, an inhibitor of Pol II transcription (Figures 1G, 1I, S1C, and S1D). Likewise, depletion of XRCC1, which also decreased the levels of DNA ligase 3 (Figure 1J; Caldecott et al., 1995), induced a MG132- and flavopiridol-sensitive increase of γH2AX and/or p53BP1 foci in response to CPT (Figures 1K and S1E). Together, these results indicate that the SSB intermediates produced during the removal of transcription-blocking TOP1ccs give rise to DSBs in non-replicating cells.

The Formation of Transcriptional DSBs Depends on R-Loops

A possible mechanism for the formation of DSBs in non-replicating cells is that the SSB intermediate produced during the removal of a transcription-blocking TOP1cc would be converted into a DSB by a nearby SSB on the opposing DNA strand. Notably, R-loop structures that form co-transcriptionally in an unscheduled manner are prone to DNA breakage (Aguilera and Gómez-González, 2017; Sollier and Cimprich, 2015). We therefore determined whether R-loops could be linked to the production of a SSB on the opposing DNA strand.

Although TOP1 depletion is known to increase R-loop levels (Drolet et al., 2003; El Hage et al., 2010; Manzo et al., 2018; Tuduri et al., 2009), the effect of TOP1cc trapping on R-loops is still unclear. To address this, quiescent cells were exposed to CPT and R-loop levels were assessed by a DNA slot blot assay employing S9.6 antibody (Boguslawski et al., 1986). CPT did not significantly affect S9.6 signal, albeit a small and transient increase was observed after 5 min, consistent with previous reports (Figures 2A and 2B; Marinello et al., 2013, 2016). RNase H treatment suppressed S9.6 signal, indicating its specificity for RNA/DNA hybrids (Figures 2A and 2B). These results indicate that TOP1cc trapping does not significantly increase R-loop levels. We therefore hypothesized that TOP1cc trapping

Figure 1. Depletion of PNKP, DNA Ligase 3, or XRCC1 Increases CPT-Induced Transcription- and Proteasome-Dependent DSBs in Quiescent Cells
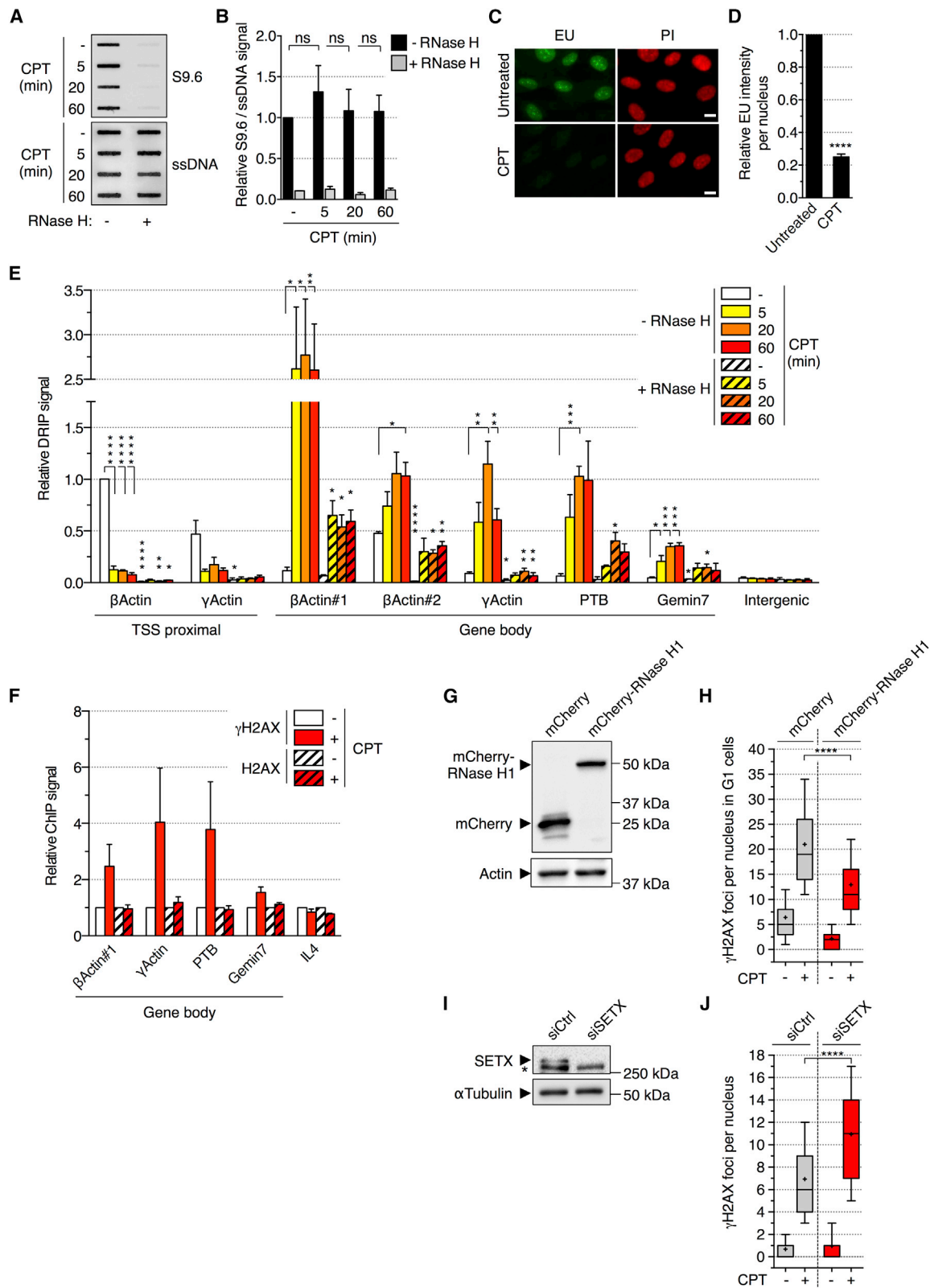
(A and B) Quiescent cells were treated with CPT (25 μM; 1 h) and co-stained for γH2AX (green) and p53BP1 (red).

(A) Representative confocal microscopy pictures. Yellow indicates colocalization. Dashed lines indicate nuclei. Scale bars: 10 μm.

(B) Number of γH2AX and p53BP1 foci per nucleus. ****$p < 0.0001$ (one-way ANOVA).

(C and D) Detection of DSBs by neutral comet assays in quiescent cells treated with CPT (25 μM; 1 h).

(C) Representative pictures of nuclei.

(D) Quantification of neutral comet tail moments. ****$p < 0.0001$ (two-tailed unpaired t test).

(E) Pathway for the removal of a transcription-blocking TOP1cc. Y: TOP1 catalytic tyrosine.

(F–K) Quiescent cells were transfected with the indicated siRNAs.

(F, H, and J) Western blot probed with PNKP (F), Ligase 3 (H), and XRCC1 and Ligase 3 (J). α-tubulin, KAP1: loading controls.

(G, I, and K) Cells transfected with siRNAs against PNKP (G), Ligase 3 (I), and XRCC1 (K) were treated with MG132 (25 μM) or flavopiridol (1 μM) for 1 h before the addition of CPT (25 μM; 1 h) and co-stained for γH2AX and p53BP1. The number of γH2AX foci per nucleus is shown. ****$p < 0.0001$ (one-way ANOVA).

(B, D, G, I, and K) A representative experiment out of ≥3 is shown.

See also Figure S1.

could instead cause a genomic redistribution of R-loops. In support to this possibility, CPT readily inhibited transcription (Figures 2C and 2D; Cristini et al., 2016; Desai et al., 2003) and therefore could decrease the levels of physiological R-loops that have a rapid turnover (∼10–20 min) and are enriched 1 to 2 kb downstream of transcription start site (TSS) of expressed genes (Sanz et al., 2016). Conversely, CPT could increase R-loops in the body of genes where it primarily traps TOP1ccs and blocks transcription (Baranello et al., 2016; Solier et al., 2013; Sordet et al., 2008).

Therefore, we examined R-loops at the TSS-proximal and gene body regions using RNA/DNA hybrid immunoprecipitation

(legend on next page)

(DRIP) with the S9.6 antibody. Consistent with the prevalent localization of physiological R-loops at promoter-proximal regions (Sanz et al., 2016; Skourti-Stathaki et al., 2011), RNase H-sensitive DRIP signals were detected at TSS-proximal regions of β-actin and γ-actin genes in untreated quiescent cells (Figure 2E, white bars). CPT induced a rapid drop of DRIP signals at TSS-proximal regions together with an increase in the body of these genes (Figure 2E). Such increase of DRIP signals was also observed over PTB and Gemin7 genes (Figure 2E). These results indicate that TOP1cc trapping by CPT treatment increases R-loop levels over gene bodies.

To assess the role of R-loops in TOP1cc-dependent transcriptional DSBs, we investigated whether R-loops form at DSB sites. Chromatin immunoprecipitation (ChIP) analysis showed an enrichment of γH2AX after CPT exposure on β-actin, γ-actin, PTB, and Gemin7 genes (Figure 2F), coinciding with positions of R-loop enrichment (Figure 2E). To assess the direct consequences of R-loops, we tested whether modulating their cellular levels could impact DSB formation. First, we decreased R-loops by overexpressing RNase H1. We took advantage of U2OS cells inducible for mCherry or mCherry-RNase H1 fusion protein (Figure 2G; Britton et al., 2014). These cells cannot enter quiescence; hence, we analyzed DSBs in G1, prior to DNA replication. CPT-induced DSBs in G1 cells were also dependent on transcription and TOP1 degradation (Figure S2A), indicating that these DSBs are produced by a mechanism similar to quiescent cells (Figures 1 and S1). RNase H1 overexpression decreased the number of γH2AX foci induced by CPT in G1 cells (Figure 2H). Second, we increased R-loops by depleting SETX or AQR (Groh et al., 2017; Skourti-Stathaki et al., 2011; Sollier et al., 2014). Small interfering RNA (siRNA)-mediated knockdown of SETX or AQR increased the number of γH2AX and p53BP1 foci in CPT-treated quiescent cells (Figures 2I, 2J, and S2B–S2D). SETX depletion also increased DRIP signals over β-actin, PTB, and Gemin7 genes (Figure S2E). Together, these data indicate that R-loops contribute to the formation of TOP1cc-induced transcriptional DSBs in non-replicating cells.

Structure-Specific Endonucleases Cleave R-Loops to Produce Transcriptional DSBs

Next, we asked whether the SSBs in R-loops could contribute to DSB production. Because R-loops form single-stranded DNA structures with flap extremities, we tested whether the inhibition of structure-specific endonucleases that can cleave related structures can prevent the induction of DSBs in CPT-treated quiescent cells. XPF, XPG, FEN1, MRE11, ARTEMIS, CtIP, and MUS81 all possess flap endonuclease activity (Dehé and Gaillard, 2017; Regairaz et al., 2011). RNAi-mediated depletion of XPF, XPG, FEN1, or MRE11, but not of ARTEMIS, CtIP, or MUS81, reduced the induction of γH2AX and p53BP1 foci by CPT (Figures 3 and S3). These results support a role for R-loop cleavage in the production of TOP1cc-mediated transcriptional DSBs and further suggest that these breaks can be mediated by several endonucleases, including XPF, XPG, FEN1, and MRE11. To further examine the mechanism of endonuclease-mediated R-loop cleavage in the production of these DSBs, we initially focused on XPF because its depletion had the most severe defect in DSB induction (Figures 3 and S3).

We first asked whether XPF is recruited to R-loops in response to CPT. ChIP analysis in quiescent cells showed an enrichment of XPF after CPT treatment over β-actin, γ-actin, PTB, and Gemin7 genes (Figure 4A), coinciding with R-loop accumulation (Figure 2E). To test whether XPF binds to R-loops, we used the R-loop immunoprecipitation (IP) method we recently developed, which allows the identification of RNA/DNA hybrid-interacting proteins in cells (Figure 4B; Cristini et al., 2018). XPF was enriched in RNA/DNA hybrid IP samples compared to the nuclear lamin B protein and "no antibody" IP samples in untreated quiescent cells (Figure 4C), indicating that XPF binds to R-loops under physiological conditions. Cellular exposure to CPT resulted in a further enrichment of XPF in the RNA/DNA hybrid IP (Figures 4C and 4D), and the quantity of RNA/DNA hybrid IPs was comparable (Figure S4A). The interaction of XPF with RNA/DNA hybrids is specific as it was reduced by RNase H treatment and prevented by synthetic RNA/DNA hybrid competitors added into IP reaction (Figures

---

Figure 2. CPT Induces R-Loop-Dependent DSBs in the Absence of DNA Replication

(A and B) RNA/DNA hybrid slot blot of genomic DNA ± RNase H from quiescent cells treated with 25 μM CPT.

(A) Representative slot blot. ssDNA: loading control.

(B) Values are normalized to ssDNA (means ± SEM; n ≥ 2). not significant (ns; two-tailed unpaired t test).

(C and D) Immunofluorescence (IF) analysis of 5-ethynyl uridine (EU) incorporation in quiescent cells treated with CPT (25 μM; 1 h) and incubated with 1 mM EU for the last 30 min of CPT treatment.

(C) Representative pictures. EU (green); propidium iodide (PI; red); scale bars: 10 μm.

(D) Values are normalized to untreated cells (means ± SEM; n = 3). ****$p < 0.0001$ (two-tailed unpaired t test).

(E) DRIP analysis in quiescent cells treated with 25 μM CPT. Values are normalized to β-actin "TSS proximal" amplicon of the "−RNase H" sample from untreated cells (means ± SEM; n = 3). *$p < 0.05$, **$p < 0.01$, ***$p < 0.001$, ****$p < 0.0001$ (two-tailed unpaired t test). Intergenic: negative control.

(F) γH2AX and H2AX ChIP analysis in quiescent cells treated with CPT (25 μM; 1 h). Values are normalized to untreated cells (means ± SEM; n ≥ 2). Interleukin-4 (IL-4): negative control.

(G and H) U2OS cells were treated with doxycycline to express mCherry or mCherry-RNase H1.

(G) Western blot of mCherry. Actin: loading control.

(H) Cells were incubated with 10 μM EdU for 30 min before treatment with CPT (25 μM; 1 h) and stained for γH2AX and Hoechst 33342 (DNA). The number of γH2AX foci per G1 nucleus (EdU-negative and low Hoechst 33342) is shown.

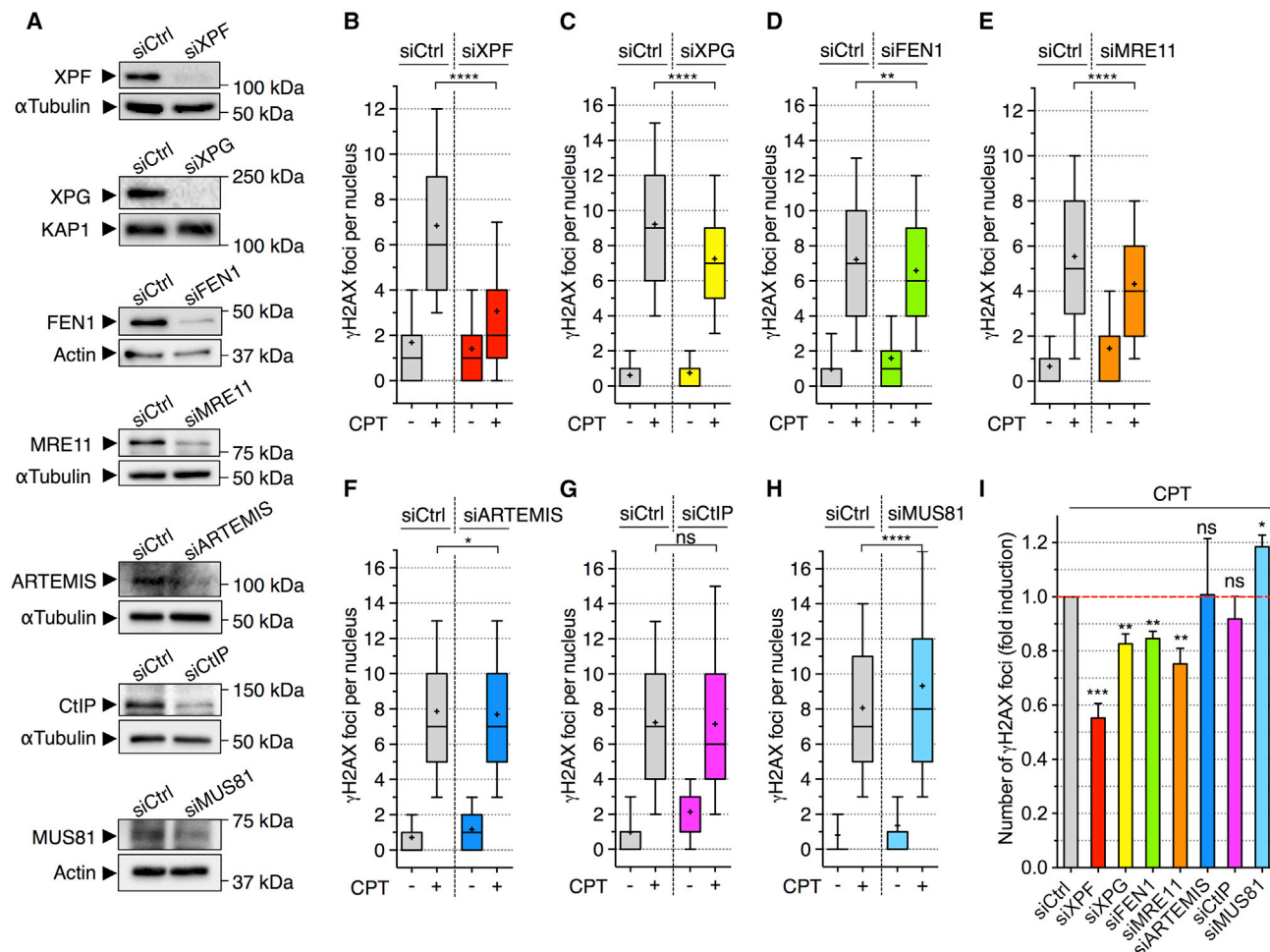(I and J) Quiescent cells were transfected with siCtrl or siSETX.

(I) Western blot of SETX. *non-specific band. α-tubulin: loading control.

(J) siRNA-transfected cells were treated with CPT (25 μM; 1 h) and co-stained for γH2AX and p53BP1. The number of γH2AX foci per nucleus is shown.

A representative experiment out of 2 (H) or 3 (J) is shown. ****$p < 0.0001$ (two-tailed unpaired t test).

See also Figure S2.

Figure 3. Depletion of the Nucleases XPF, XPG, FEN1, and MRE11 Reduces the Induction of DSBs in CPT-Treated Quiescent Cells
Quiescent cells were transfected with the indicated siRNAs.
(A) Western blot probed with the indicated antibodies. Actin, α-tubulin, and KAP1: loading controls.
(B–H) Cells transfected with siRNAs against XPF (B), XPG (C), FEN1 (D), MRE11 (E), ARTEMIS (F), CtIP (G), and MUS81 (H) were treated with CPT (25 μM; 1 h) and co-stained for γH2AX and p53BP1. The number of γH2AX foci per nucleus is shown. A representative experiment out of ≥3 is shown. The data with siCtrl cells in (D) and (G) are from the same experiment. ns, *p < 0.05, **p < 0.01, ****p < 0.0001 (two-tailed unpaired t test).
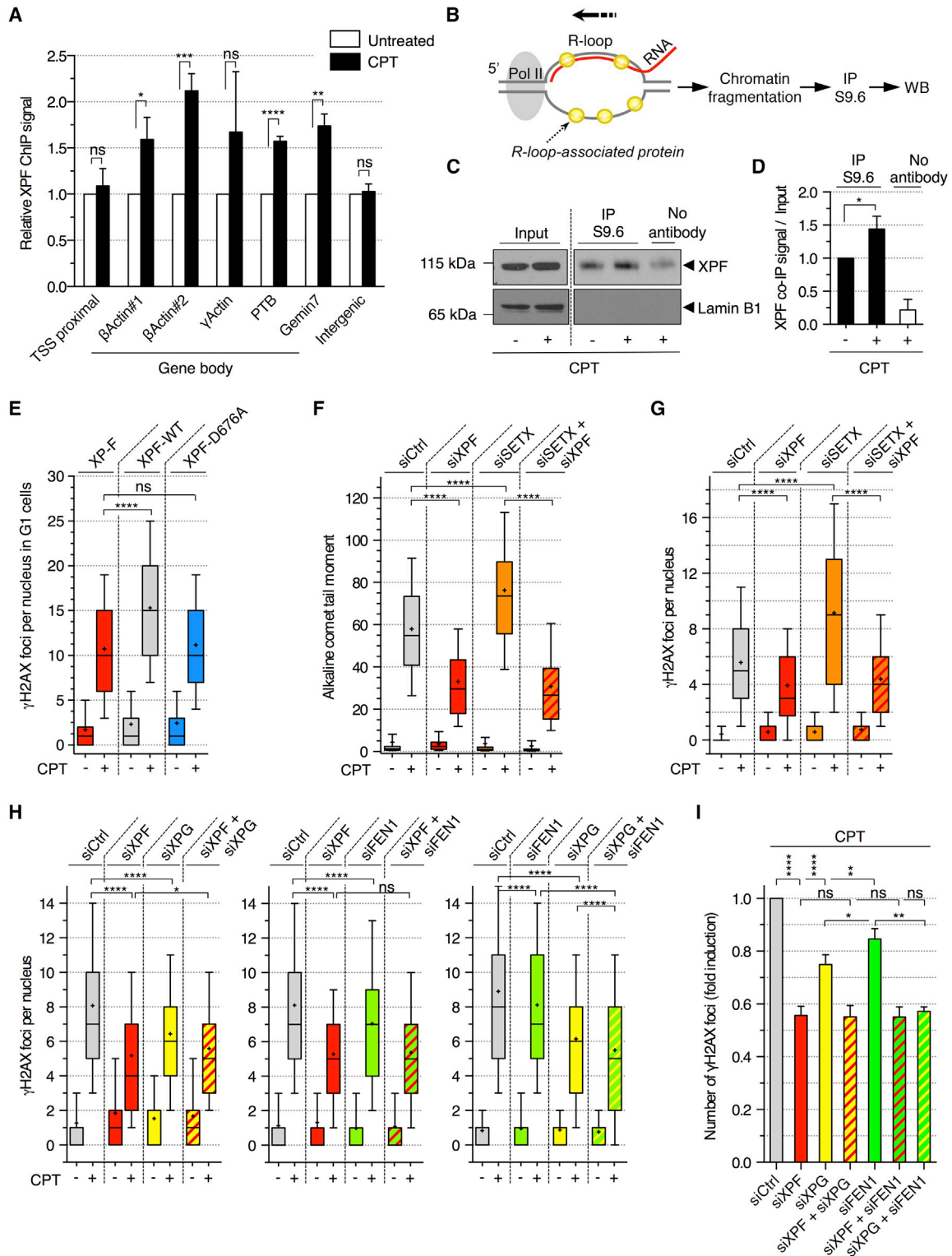(I) The fold induction of γH2AX was calculated by subtracting the number of foci of untreated cells from that of CPT-treated cells and normalized to siCtrl cells treated with CPT (means ± SEM; n ≥ 3). ns, *p < 0.05, **p < 0.01, ***p < 0.001 (two-tailed unpaired t test).
See also Figure S3.

S4B–S4D). These results indicate that XPF is enriched on gene body R-loops in response to CPT in non-replicating cells.

To determine whether XPF cleaves R-loops to produce DSBs, we tested whether the endonuclease activity of XPF is required for this process. We analyzed γH2AX induction by CPT in the G1 population of XPF-deficient cells (XP-F) complemented with either a wild-type (XPF-WT) or a nuclease-dead (XPF-D676A) XPF (Staresincic et al., 2009). CPT increased the number of γH2AX foci in XPF-WT cells compared to XPF-deficient cells, and this increase was lost in XPF-nuclease-dead cells (Figure 4E). Thus, the nuclease activity of XPF is required for the production of TOP1cc-dependent transcriptional DSBs. To further test whether XPF cleaves R-loops, we analyzed the effects of XPF depletion on R-loop-dependent DNA breaks. By using alkaline comet assays to

detect SSBs, we showed that increasing R-loop levels upon RNAi-mediated depletion of SETX resulted in an increase of SSBs in CPT-treated quiescent cells (Figure 4F). Such increase was suppressed by XPF depletion (Figure 4F), suggesting that XPF induces SSBs within R-loops. To evaluate the contribution of XPF-mediated R-loop cleavage to the formation of DSBs, we carried out the same experiments but analyzed DSBs instead of SSBs. XPF depletion also suppressed the increase of γH2AX foci induced by CPT upon SETX depletion (Figure 4G). Similar results were obtained by increasing R-loops upon AQR depletion (Figure S4E). Conversely, decreasing R-loops by RNase H1 overexpression did not further decrease the induction of γH2AX by CPT upon XPF depletion in the G1 population of U2OS cells (Figure S4F). Taken together, these results indicate that XPF can cleave

Figure 4. R-Loop-Dependent DSBs Are Mediated by XPF, XPG, and FEN1 in Non-replicating Cells Treated with CPT

(A) ChIP analysis of XPF in quiescent cells treated with CPT (25 μM; 20 min). Values are normalized to untreated cells (means ± SEM; n = 4). ns, *p < 0.05, **p < 0.01, ***p < 0.001, ****p < 0.0001 (two-tailed unpaired t test). Intergenic: negative control.

(B) R-loop IP method for the detection of R-loop-associated proteins.

(C and D) R-loop IP was carried out in quiescent cells treated with CPT (25 μM; 20 min). Input and IP fractions were probed with XPF or lamin B1 antibodies.

(legend continued on next page)

R-loops formed upon TOP1cc trapping and that such cleavage can generate DSBs independently of replication.

To assess whether XPG and FEN1 act on the same R-loops as XPF to induce DSB formation, we depleted these endonucleases in combination in quiescent cells. Co-depletion of XPF with XPG or FEN1 did not further decrease the number of γH2AX foci induced by CPT than the depletion of XPF alone (Figures 4H, left and middle panels, 4I, and S4G), suggesting that XPF and XPG, as well as XPF and FEN1, act on the same R-loops. The FEN1 nuclease inhibitor myricetin (Ma et al., 2019) decreased the induction of γH2AX and p53BP1 foci by CPT (Figures S4H and S4I), further supporting the role of FEN1 in the cleavage of R-loops. Because XPF possesses a 3′-flap endonuclease activity and XPG and FEN1 a 5′-flap endonuclease activity (Dehé and Gaillard, 2017), these results suggest that R-loops are cleaved at both 3′- and 5′-extremities to induce DSB formation in CPT-treated quiescent cells. Then, the two 5′-flap endonucleases, XPG and FEN1, were depleted together to assess whether they act on the same R-loops. Co-depletion of XPG and FEN1 showed an additive effect in decreasing the number of γH2AX foci induced by CPT (Figures 4H, right panel, and 4I), suggesting that XPG and FEN1 act on different R-loops. Notably, co-depletion of XPG and FEN1 decreased the number of γH2AX to the same extent as the depletion of XPF alone (Figure 4I), further suggesting that XPG and FEN1 are the main 5′-flap endonucleases that act with the 3′-flap endonuclease XPF on the R-loops. Taken together, these results suggest that R-loops are cleaved at both extremities by a dual incision mediated by XPG and XPF or FEN1 and XPF to induce the formation of co-transcriptional DSB in CPT-treated quiescent cells.

The Formation of Transcriptional DSBs Requires the Dual Processing of TOP1ccs and R-Loops

Our data are consistent with the possibility that, in non-replicating cells, the SSB intermediates produced during the removal of transcription-blocking TOP1ccs are converted into DSBs by the presence of nearby SSBs on opposing DNA strand generated by the cleavage of R-loops. However, another possibility is that the endonucleases cleave R-loops on both strands, generating DSBs independently of TOP1cc-dependent SSB intermediates.

To distinguish between these two possibilities, we tested whether R-loop-dependent DSBs were also dependent on SSBs generated during TOP1cc removal. We therefore induced R-loop-dependent DSBs by depleting SETX in CPT-treated quiescent cells while inhibiting TOP1 proteolysis with proteasome inhibitors to prevent the formation of TOP1cc-induced SSB intermediates (Figure 1E; Ashour et al., 2015; Pommier et al., 2014). Proteasome inhibitors MG132 and bortezomib suppressed the induction of γH2AX foci by CPT upon SETX depletion (Figure 5A). Although SETX can be recruited at DSBs (Cohen et al., 2018), ChIP analysis showed that MG132 did not prevent SETX recruitment at the β-actin, γ-actin, and PTB genes (Figure S5), indicating that SETX recruitment to these loci is not due to DSBs but rather due to the presence of R-loops. Consistent with that, MG132 also did not reduce R-loop levels measured by DNA slot blot (Figures 5B and 5C) and by DRIP (Figure 5D), excluding the possibility that fewer R-loops account for the lack of DSB induction. In addition, alkaline comet assays showed that MG132 did not prevent the induction of SSBs within the R-loops (Figure 5E). These results indicate that, in non-replicating cells, the cleavage of R-loops alone is insufficient to generate DSBs and that it requires the formation of SSB intermediates produced during the removal of TOP1ccs. Altogether, these results support a model where, in non-replicating cells, a transcription-blocking TOP1cc is converted into a DSB by the presence of two SSBs on opposing DNA strand: one SSB resulting from TOP1cc removal and the other from cleavage of an R-loop by endonucleases.

Removal of TOP1ccs and R-Loops Allows the Repair of Transcriptional DSBs

Based on this model, TDP1-deficient cells should have DSBs with 3′-DNA broken strands attached to TOP1 peptides (i.e., TOP1 partially proteolyzed; see Figure 1E), which is likely to prevent DSB repair. Indeed, the DNA end must be cleansed to allow DSB repair by non-homologous end joining (NHEJ) (Kawale et al., 2018; Menon and Povirk, 2016), which is the main repair pathway in G0/G1 cells (Hendrickson, 1997). Similarly, cells with deficiencies in R-loop resolution factors, such as SETX, will have persistent RNA/DNA hybrids between the two SSBs, which would need to be resolved to allow DSB repair. Our next question was therefore whether cells deficient for one of these pathways, in addition to forming higher levels of transcriptional DSBs, would also be unable to repair them. We therefore analyzed the effects of TDP1 and SETX depletion on the repair of CPT-induced transcriptional DSBs.

To determine the kinetics of DSB repair, we analyzed the reversal kinetics of DSB-associated foci (Löbrich et al., 2010). Cells were exposed to CPT, washed free of drug, and

(C) Representative immunoblots.

(D) Quantification of R-loop IP. Values were normalized to input and DMSO sample (means ± SEM; n = 3). *p < 0.05 (two-tailed unpaired t test).

(E) XPF-deficient patient cell line (XP-F) complemented with a wild-type (XPF-WT) or a nuclease-dead (XPF-D676A) XPF were incubated with 10 μM EdU for 30 min before treatment with CPT (25 μM; 1 h) and stained for γH2AX and Hoechst 33342 (DNA). The number of γH2AX foci per G1 nucleus (EdU-negative and low Hoechst 33342) is shown. ns, ****p < 0.0001 (two-tailed unpaired t test).

(F–I) Quiescent cells were transfected with the indicated siRNAs and treated with CPT (25 μM; 1 h).

(F) Detection of SSBs by alkaline comet assays. The quantification of comet tail moments is shown. ****p < 0.0001 (one-way ANOVA).
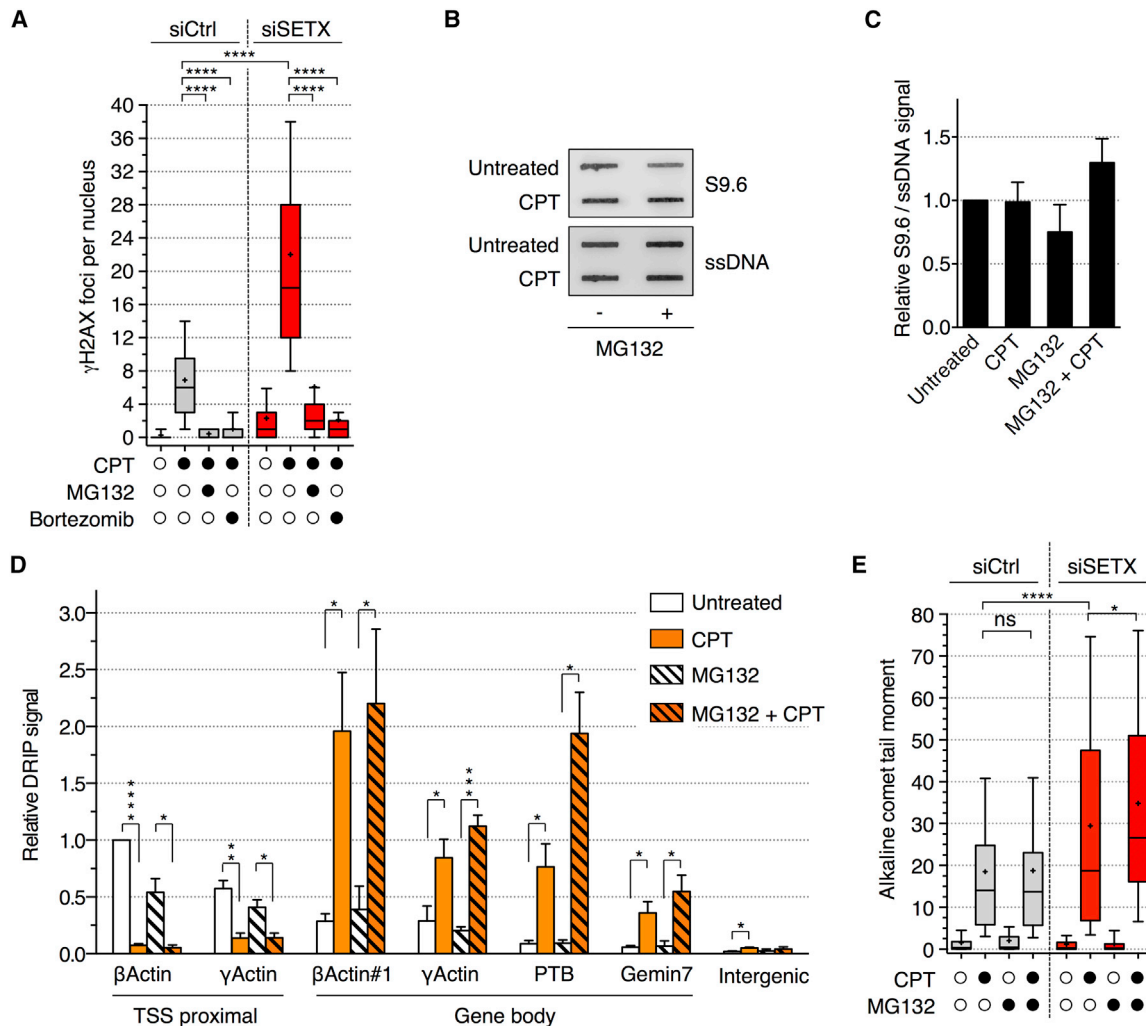
(G) Number of γH2AX foci per nucleus. ****p < 0.0001 (one-way ANOVA).

(H) Number of γH2AX foci per nucleus. ns, *p < 0.05, ****p < 0.0001 (one-way ANOVA).

(I) The fold induction of γH2AX was calculated by subtracting the number of foci of untreated cells from that of CPT-treated cells and normalized to siCtrl cells treated with CPT in each experiment (means ± SEM; n ≥ 3). ns, *p < 0.05, **p < 0.01, ****p < 0.0001 (two-tailed unpaired t test).

A representative experiment out of 2 (E and G) or ≥3 (F and H) is shown.

See also Figure S4.

Figure 5. Proteasome Inhibition Prevents R-Loop-Dependent DSBs in CPT-Treated Quiescent Cells

(A) Quiescent cells were transfected with siCtrl or siSETX, treated with MG132 (25 μM; 1 h) or bortezomib (1 μM; 4 h) before the addition of CPT (25 μM; 1 h), and stained for γH2AX. The number of γH2AX foci per nucleus is shown.

(B and C) RNA/DNA hybrid slot blot of genomic DNA from quiescent cells treated with MG132 (10 μM; 1 h) before the addition of CPT (25 μM; 1 h), probed with S9.6 and ssDNA antibodies.

(B) Representative slot blot. ssDNA: loading control.

(C) Quantification of RNA/DNA hybrid slot blot. Values are normalized to ssDNA (means ± SEM; n = 4).

(D) DRIP analysis from quiescent cells treated as in (B) and (C). Values are normalized to β-actin TSS proximal from untreated cells (means ± SEM; n = 3). *p < 0.05, **p < 0.01, ***p < 0.001, ****p < 0.0001 (two-tailed unpaired t test).

(E) Detection of SSBs by alkaline comet assays in cells transfected and treated as in (A). The quantification of comet tail moments is shown.

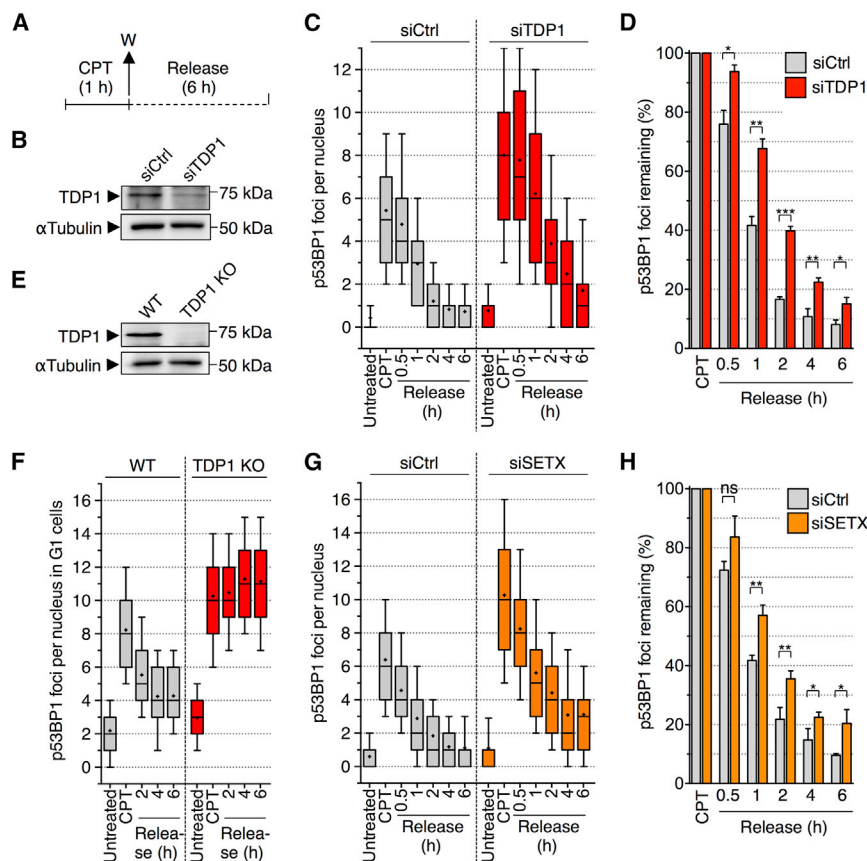A representative experiment out of 2 is shown in (A) and (E); ns, *p < 0.05, ****p < 0.0001 (one-way ANOVA).

See also Figure S5.

γH2AX/p53BP1 foci were monitored post-CPT treatment (Figure 6A) as reported (Mamouni et al., 2014). In quiescent cells, the number of γH2AX and p53BP1 foci decreased rapidly after CPT removal. However, reversal kinetic was faster for p53BP1 foci than for γH2AX foci (Figures S6A and S6B). Neutral comet assays showed a reversal of about 80%, 1 h after CPT removal (Figures S6C and S6D), which correlates with p53BP1 reversal kinetics. Therefore, we chose p53BP1 to study DSB repair.

RNAi-mediated depletion of TDP1 led to persistent p53BP1 foci after CPT removal in quiescent cells (Figures 6B–6D). Such

a defect in p53BP1 reversal kinetics was also observed in the G1 population of HCT116 cells knockout (KO) for TDP1 (Figures 6E and 6F). Similarly, RNAi-mediated depletion of SETX led to persistent p53BP1 foci after CPT removal in quiescent cells (Figures 6G and 6H). These results indicate that cells deficient for TOP1cc removal or R-loop resolution form high levels of transcriptional DSBs due to their defective repair.

Besides NHEJ, DSBs can be repaired in G0/G1 cells by the single-strand annealing (SSA) pathway. SSA consists of the annealing of homologous repeat sequences and requires the

Figure 6. TDP1- and SETX-Deficient Cells Are Defective for the Repair of CPT-Induced Non-replicating DSBs

(A) Protocol to study p53BP1 foci reversal following CPT removal used in (C), (D), and (F)–(H). Cells were treated with CPT (25 μM; 1 h), washed (W), and cultured in CPT-free medium for up to 6 h (release).

(B–D) Quiescent cells were transfected with siCtrl or siTDP1.

(B) Western blot of TDP1. α-tubulin: loading control.

(C) Number of p53BP1 foci per nucleus.

(D) The percentages of p53BP1 foci remaining following CPT removal were calculated by subtracting the number of foci of untreated cells from that of treated cells and normalized to cells treated with CPT (means ± SEM; n = 4). *p < 0.05, **p < 0.01, ***p < 0.001 (two-tailed unpaired t test).

(E) Western blot of TDP1 in TDP1 WT and TDP1 KO HCT116 cells.

(F) p53BP1 foci in G1 nuclei (EdU-negative and low Hoechst 33342) of TDP1 WT and TDP1 KO HCT116 cells.

(G) Similar experiment as in (C) in quiescent cells transfected with siSETX.

(H) Similar experiment as in (D) in quiescent cells transfected with siSETX. Means ± SEM; n = 3. ns, *p < 0.05, **p < 0.01 (two-tailed unpaired t test).

A representative experiment out of ≥2 is shown in (C), (F), and (G).

See also Figure S6.

RAD52 protein (Ceccaldi et al., 2016). RNAi-mediated depletion of RAD52 in quiescent cells did not affect the reversal kinetics of p53BP1 foci upon CPT removal (Figures S6E and S6F). These results suggest that, in quiescent cells, transcriptional DSBs are not repaired by the SSA pathway, thus supporting repair by NHEJ.

TOP1cc- and R-Loop-Dependent Transcriptional DSBs Accumulate under Physiological Conditions

CPT selectively traps TOP1ccs (Nitiss and Wang, 1988; Pommier, 2006), and hence, it is a precise tool to dissect the production mechanism of TOP1cc-dependent transcriptional DSBs. Besides CPT, a wide range of DNA alterations can trap TOP1ccs, and many of them are frequent (Pommier et al., 2016). To determine whether transcriptional DSBs could form under physiological conditions by a mechanism that relies on TOP1ccs and R-loop processing, we analyzed DSBs in quiescent cells under normal cultured conditions without CPT.
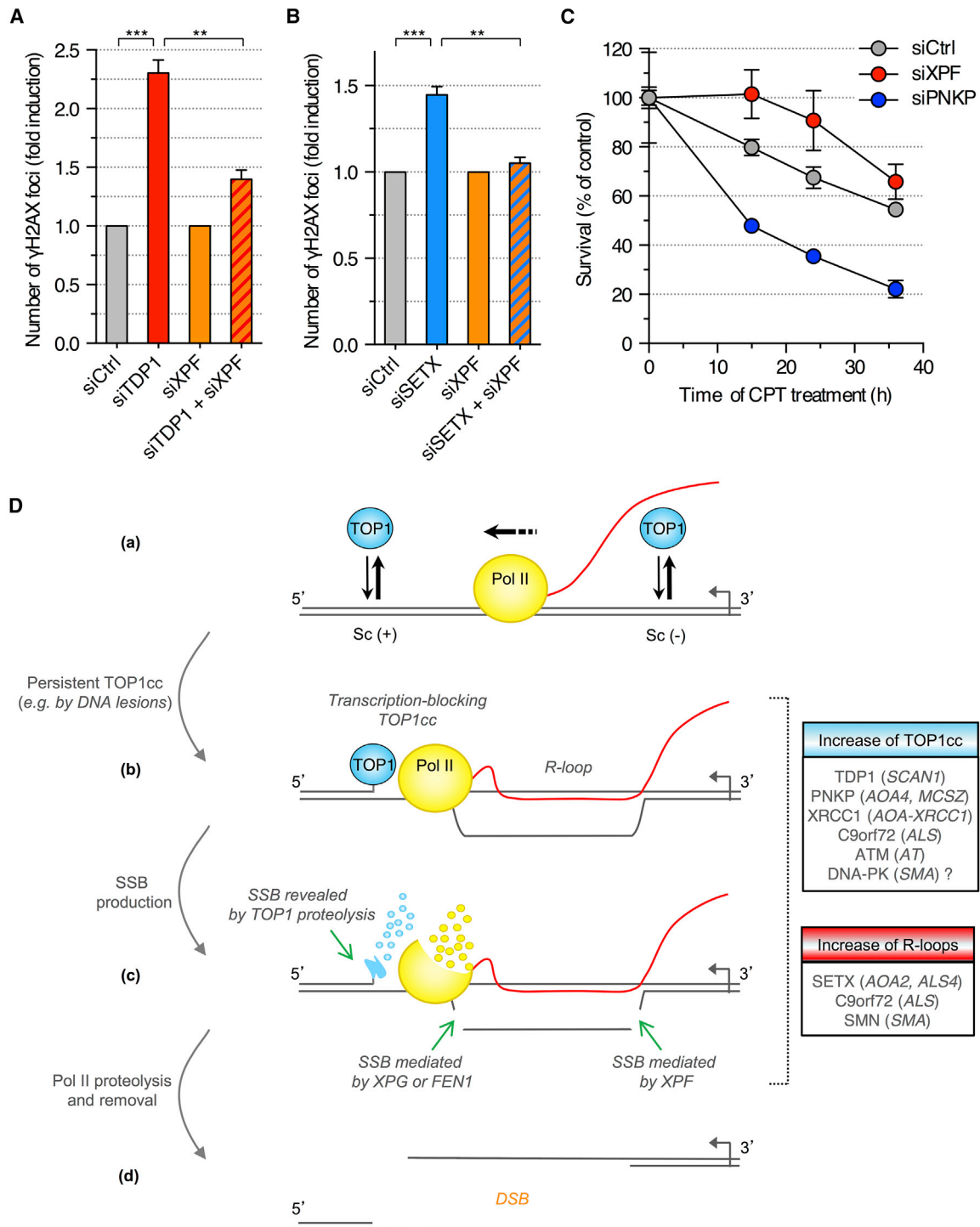
RNAi-mediated depletion of TDP1 (Figure 6B) increased the number of γH2AX and p53BP1 foci (Figures 7A, S7A, and S7C), indicating that SSB intermediates produced during TOP1cc removal promote DSB formation. Concurrent depletion of XPF suppressed the induction of γH2AX and p53BP1 foci upon TDP1 knockdown (Figures 7A, S7A, and S7C), suggesting that DSBs formed upon depletion of TDP1 depend on SSBs within the R-loops. To control that XPF cleaves R-loops to

form DSBs, we increased R-loop levels and prevented their cleavage by depletion of SETX and XPF, respectively. The increase of γH2AX and p53BP1 foci upon depletion of SETX was abrogated by the concurrent depletion of XPF (Figures 7B, S7B, and S7C). Together, these results led us to conclude that TOP1cc-dependent transcriptional DSBs form under physiological conditions and involve the dual processing of TOP1cc and R-loops.

To assess whether these transcriptional DSBs affect the viability of non-replicative cells, we tested the effect of CPT-dependent DSB formation on the survival of quiescent cells. Increasing DSBs by depleting PNKP with siRNA (Figures 1F and 1G) decreased cell survival in response to CPT (Figure 7C), whereas decreasing DSBs by depleting XPF with siRNA (Figures 3A and 3B) increased cell survival (Figure 7C). These results highlight the physiological relevance of transcription-dependent DSBs induced by the dual processing of TOP1ccs and R-loops in non-replicating cells.

DISCUSSION

Genomic instability in resting cells is an emerging cause of neurodegenerative syndromes. Even so, our understanding of how DSBs are produced in non-replicating cells is limited. Here, we report a mechanism of DSB formation that strictly depends on transcription. DSBs are generated by two nearby SSBs

Figure 7. Depletion of XPF Prevents the Induction of DSBs upon Depletion of TDP1 in Quiescent Cells

(A and B) Quiescent cells were transfected with the indicated siRNAs and co-stained for γH2AX and p53BP1. To compare XPF-proficient (siCtrl) and XPF-deficient (siXPF) cells upon depletion of TDP1 (A) or SETX (B), γH2AX induction was normalized to 1 in both siCtrl and siXPF cells (means ± SEM; n = 3). **p < 0.01, ***p < 0.001 (two-tailed unpaired t test).

(C) Viability of siRNA-transfected quiescent cells treated with 25 μM CPT (means ± SEM of triplicates).

(D) Model for the induction of DSBs during transcription. (a) TOP1 removes both positive and negative DNA supercoiling (Sc) generated during transcription. (b) Stabilization of a TOP1cc on the template strand blocks Pol II transcription and promotes R-loop formation. (c) The transcription-blocking TOP1cc is partially proteolyzed by the ubiquitin-proteasome system, which reveals the SSB. The R-loop is cleaved by a dual incision mediated by XPG and XPF or FEN1 and XPF

(legend continued on next page)

on opposing DNA strands, both produced during transcription. One SSB arises from the repair of a transcription-blocking TOP1cc by the TDP1 pathway and the other from cleavage of an R-loop by endonucleases. Our data can be explained by the model in Figure 7D, where the SSB resulting from TOP1cc removal is on the transcribed DNA strand ahead of Pol II and the SSB in the R-loop is behind Pol II on the non-transcribed DNA strand displaced by the RNA/DNA hybrid. This polarity is in agreement with previous work showing that a TOP1cc located specifically on the transcribed strand blocks transcription (Bendixen et al., 1990; Wu and Liu, 1997) and is converted into an irreversible TOP1cc (Wu and Liu, 1997), the removal of which depends primarily on the TDP1 pathway (Cristini et al., 2016; El-Khamisy et al., 2005; Miao et al., 2006; Yang et al., 1996). In addition, R-loops form behind the elongating Pol II (Huertas and Aguilera, 2003), and the single-stranded nature of the displaced DNA strand within the R-loop makes it more vulnerable to DNA damage (Sollier and Cimprich, 2015).

An alternative model could be that the SSB generated during TOP1cc removal is located on the RNA/DNA hybrid within the R-loop or a few base pairs away from it. This is plausible as TOP1 removes negative DNA supercoiling behind the elongating Pol II (Pommier et al., 2016) and TOP1 co-immunoprecipitates with RNA/DNA hybrids (Cristini et al., 2018). However, it has not been reported that CPT can trap TOP1ccs in RNA/DNA hybrids and, if so, whether this would lead to irreversible TOP1ccs, the removal of which would depend on TDP1. Nevertheless, our results showing that the production of SSBs at R-loops is suppressed by XPF depletion (Figure 4F) argue against the possibility that TOP1ccs generate SSBs in RNA/DNA hybrids in our cell model.

Our data support that CPT increases R-loops in gene bodies, which is consistent with previous work showing that this is where TOP1ccs are primarily trapped (Baranello et al., 2016; Solier et al., 2013). Persistent TOP1ccs represent a barrier to the elongating Pol II (Bendixen et al., 1990; Sordet et al., 2008; Wu and Liu, 1997), which could promote R-loop formation by displacing spliceosomes (Tresini et al., 2015). Also, TOP1ccs could favor R-loop formation by increasing non-coding RNAs, such as antisense RNAs (Graf et al., 2017; Marinello et al., 2013, 2016; Nojima et al., 2018). A recent genome-wide analysis following TOP1 depletion shows R-loop gains in gene bodies (Manzo et al., 2018), suggesting that the decrease in TOP1 activity could also account for the effects of CPT on R-loops. Such a decrease in TOP1 activity could promote R-loop formation as a result of negative supercoiling accumulating behind the elongating Pol II (Drolet et al., 2003) and/or inhibition of the serine and arginine-rich (SR)-kinase activity of TOP1 interfering with splicing (Li and Manley, 2005; Tuduri et al., 2009).

Unscheduled R-loops can induce DSBs and genomic instability (Aguilera and García-Muse, 2012; Sollier and Cimprich, 2015). Our analysis in non-replicating cells suggests that a DSB does not form directly in the R-loop by the cleavage of both strands. Instead, a SSB is produced on the displaced DNA strand within the R-loop and the DSB is created by a second SSB next to the R-loop on the opposing DNA strand. In replicating cells, it is also plausible that a SSB within the R-loop could be converted into a DSB as the DNA replicates. Our data show that the SSB in the R-loop is mediated by the nucleases XPF, XPG, and FEN1. Consistently, XPF and XPG have been reported to cleave R-loops *in vitro* (Tian and Alt, 2000) and in cells (Sollier et al., 2014; Yasuhara et al., 2018), and FEN1 contributes to R-loop resolution during telomere replication (Teasley et al., 2015). XPF has a 3′-flap endonuclease activity, whereas XPG and FEN1 have a 5′-flap activity (Dehé and Gaillard, 2017). Our results from nuclease co-depletion experiments support a model in which R-loops are cleaved at both 3′- and 5′-extremities to induce DSBs by a dual incision mediated by XPF and XPG or XPF and FEN1. Although the cleavage at both ends of the R-loops might occur independently of each other, it is possible that it is more coordinated, e.g., that the cleavage at one end primes the cleavage at the other end. Although MRE11 is primarily involved in DSB repair by homologous recombination (Ceccaldi et al., 2016), it is unlikely that it contributes to the repair of transcriptional DSBs in quiescent cells due to the absence of sister chromatids for recombination. MRE11 has both an endonuclease and an exonuclease activity. It may therefore promote DSB formation by cleaving R-loops and/or by resecting DNA after a break is produced. Nuclease-independent functions of MRE11 may also contribute, including recruitment and activation of ATM (Buis et al., 2008), ultimately resulting in TOP1 degradation (Katyal et al., 2014) and further induction of transcriptional DSBs (this study; Cristini et al., 2016).

Although the two SSBs on opposing DNA strands can be distant from each other, it is plausible that they give rise to a DSB because the DNA strands in between, i.e., in the R-loop and the transcription bubble, are not annealed. Previous work also reported that Pol II arrested by TOP1ccs is released from chromatin (Sordet et al., 2008) and degraded by the proteasome (Desai et al., 2003), which would enable strand separation. DNA strand separation may be further facilitated by the removal of single-stranded DNA (ssDNA) fragments of R-loops that we report here. Lastly, although the DNA strands between TOP1ccs and stalled Pol II may be annealed, their length has been estimated *in vitro* to be ~10 bp (Bendixen et al., 1990), and melting of the DNA duplex can readily occur over such a short length (Ran et al., 2013).

Non-replicative DSBs likely occur spontaneously in cells because TOP1ccs can be trapped under physiological conditions, including oxidative base damage, alkylation and nicks (Pommier et al., 2014), and ribonucleotide misincorporation (Huang et al., 2015, 2017; Kim et al., 2011; Sparks and Burgers, 2015). Consistently, our data indicate that DSBs dependent on the processing of both TOP1ccs and R-loops are produced in non-replicating cells under physiological conditions (Figures 7A and 7B). Genetic

---

generating a SSB on the opposing DNA strand. Stalled Pol II is degraded and/or removed from the chromatin. (d) The two DNA strands separate forming a DSB. Boxes indicate human disorders associated with increase of TOP1cc (blue) or R-loop levels (red). Genes mutated in these disorders are indicated. ALS, amyotrophic lateral sclerosis; AOA, ataxia with oculomotor apraxia; AT, ataxia telangiectasia; SCAN, spinocerebellar ataxia with axonal neuropathy; SMA, spinal muscular atrophy; SMN, survival motor neuron.
See also Figure S7.

defects in the transcription-blocking TOP1cc repair pathway (TDP1, PNKP, and XRCC1) and in the resolution of R-loops (SETX) are associated with genomic instability and cause neurological diseases, primarily cerebellar ataxia and amyotrophic lateral sclerosis (see Figure 7D; Dumitrache and McKinnon, 2017; Groh et al., 2017; Hoch et al., 2017; Takashima et al., 2002). This study reveals that such genetic defects enhance transcriptional DSBs in CPT-treated quiescent cells due to an increase in their production and a defect in repair. This raises the possibility that these persistent DSBs would accumulate over time, contributing to the neurodegenerative phenotype. Consistently, this study (Figure 7C) and previous work (Cristini et al., 2016) showed that such DSBs and their modulation by factors controlling their production can kill non-replicating cells. A further connection between TOP1ccs, R-loops, and neurological disease has recently been reported. Cells bearing the C9orf72 expansion repeat, the most common genetic cause of amyotrophic lateral sclerosis, accumulate both TOP1ccs and R-loops, resulting in DSBs (Walker et al., 2017). In addition, deficiency of ATM or DNA-PK, which elevates TOP1cc levels (Cristini et al., 2016; Katyal et al., 2014), can also cause neurological diseases (Kannan et al., 2018; Savitsky et al., 1995). Neurons may be prone to produce transcriptional DSBs as a result of high rates of oxygen consumption, which produces reactive oxygen species that can stabilize TOP1ccs (Daroui et al., 2004; Pommier, 2006; Pommier et al., 2014). We also note that oxidative stress has been implicated in several neurodegenerative diseases (Barnham et al., 2004). Furthermore, DSBs may be particularly deleterious in neurons due to their reduced DNA repair capability as compared to proliferating cells (Rass et al., 2007).

STAR★METHODS

Detailed methods are provided in the online version of this paper and include the following:

- KEY RESOURCES TABLE
- LEAD CONTACT AND MATERIALS AVAILABILITY
- EXPERIMENTAL MODEL AND SUBJECT DETAILS
  - Cells and Treatments
- METHOD DETAILS
  - Immunofluorescence Microscopy
  - Chromatin Immunoprecipitation (ChIP)
  - RNA/DNA Immunoprecipitation (DRIP)
  - RNA/DNA Hybrid Slot Blot
  - RNA/DNA Hybrid Co-immunoprecipitation
  - Cell Extracts and Immunoblotting
  - Comet Assays
  - siRNA Transfection
  - Quantification of Global RNA Transcription
  - Cell Viability Assays
- QUANTIFICATION AND STATISTICAL ANALYSIS
- DATA AND CODE AVAILABILITY

SUPPLEMENTAL INFORMATION

Supplemental Information can be found online at https://doi.org/10.1016/j.celrep.2019.08.041.

AUTHOR CONTRIBUTIONS

A.C. and O.S. conceived the study; N.G. and O.S. supervised the study; A.C., G.R., S.S., and O.S. performed research; S.B., S.N.H., P.C., and Y.P. provided materials and analyzed data; A.C., J.M., G.F., G.C., N.G., and O.S. analyzed data; A.C. and O.S. wrote the manuscript; and S.B., P.C., Y.P., G.F., G.C., and N.G. edited the manuscript.

DECLARATION OF INTERESTS

The authors declare no competing interests.

REFERENCES

Aguilera, A., and García-Muse, T. (2012). R loops: from transcription byproducts to threats to genome stability. Mol. Cell 46, 115–124.

Aguilera, A., and Gómez-González, B. (2017). DNA-RNA hybrids: the risks of DNA breakage during transcription. Nat. Struct. Mol. Biol. 24, 439–443.

Al Abo, M., Sasanuma, H., Liu, X., Rajapakse, V.N., Huang, S.Y., Kiselev, E., Takeda, S., Plunkett, W., and Pommier, Y. (2017). TDP1 is critical for the repair of DNA breaks induced by sapacitabine, a nucleoside also targeting ATM- and BRCA-deficient tumors. Mol. Cancer Ther. 16, 2543–2551.

Ashour, M.E., Atteya, R., and El-Khamisy, S.F. (2015). Topoisomerase-mediated chromosomal break repair: an emerging player in many games. Nat. Rev. Cancer 15, 137–151.

Baranello, L., Wojtowicz, D., Cui, K., Devaiah, B.N., Chung, H.J., Chan-Salis, K.Y., Guha, R., Wilson, K., Zhang, X., Zhang, H., et al. (2016). RNA polymerase II regulates topoisomerase 1 activity to favor efficient transcription. Cell 165, 357–371.

Barnham, K.J., Masters, C.L., and Bush, A.I. (2004). Neurodegenerative diseases and oxidative stress. Nat. Rev. Drug Discov. 3, 205–214.

Bendixen, C., Thomsen, B., Alsner, J., and Westergaard, O. (1990). Camptothecin-stabilized topoisomerase I-DNA adducts cause premature termination of transcription. Biochemistry 29, 5613–5619.

Boguslawski, S.J., Smith, D.E., Michalak, M.A., Mickelson, K.E., Yehle, C.O., Patterson, W.L., and Carrico, R.J. (1986). Characterization of monoclonal antibody to DNA.RNA and its application to immunodetection of hybrids. J. Immunol. Methods 89, 123–130.

Britton, S., Dernoncourt, E., Delteil, C., Froment, C., Schiltz, O., Salles, B., Frit, P., and Calsou, P. (2014). DNA damage triggers SAF-A and RNA biogenesis factors exclusion from chromatin coupled to R-loops removal. Nucleic Acids Res. 42, 9047–9062.

Buis, J., Wu, Y., Deng, Y., Leddon, J., Westfield, G., Eckersdorff, M., Sekiguchi, J.M., Chang, S., and Ferguson, D.O. (2008). Mre11 nuclease activity has essential roles in DNA repair and genomic stability distinct from ATM activation. Cell *135*, 85–96.

Caldecott, K.W., Tucker, J.D., Stanker, L.H., and Thompson, L.H. (1995). Characterization of the XRCC1-DNA ligase III complex in vitro and its absence from mutant hamster cells. Nucleic Acids Res. *23*, 4836–4843.

Capranico, G., Ferri, F., Fogli, M.V., Russo, A., Lotito, L., and Baranello, L. (2007). The effects of camptothecin on RNA polymerase II transcription: roles of DNA topoisomerase I. Biochimie *89*, 482–489.

Ceccaldi, R., Rondinelli, B., and D'Andrea, A.D. (2016). Repair pathway choices and consequences at the double-strand break. Trends Cell Biol. *26*, 52–64.

Cerritelli, S.M., and Crouch, R.J. (2009). Ribonuclease H: the enzymes in eukaryotes. FEBS J. *276*, 1494–1505.

Cohen, S., Puget, N., Lin, Y.L., Clouaire, T., Aguirrebengoa, M., Rocher, V., Pasero, P., Canitrot, Y., and Legube, G. (2018). Senataxin resolves RNA:DNA hybrids forming at DNA double-strand breaks to prevent translocations. Nat. Commun. *9*, 533.

Cristini, A., Park, J.H., Capranico, G., Legube, G., Favre, G., and Sordet, O. (2016). DNA-PK triggers histone ubiquitination and signaling in response to DNA double-strand breaks produced during the repair of transcription-blocking topoisomerase I lesions. Nucleic Acids Res. *44*, 1161–1178.

Cristini, A., Groh, M., Kristiansen, M.S., and Gromak, N. (2018). RNA/DNA hybrid interactome identifies DXH9 as a molecular player in transcriptional termination and R-loop-associated DNA damage. Cell Rep. *23*, 1891–1905.

Daroui, P., Desai, S.D., Li, T.K., Liu, A.A., and Liu, L.F. (2004). Hydrogen peroxide induces topoisomerase I-mediated DNA damage and cell death. J. Biol. Chem. *279*, 14587–14594.

Dehé, P.M., and Gaillard, P.H. (2017). Control of structure-specific endonucleases to maintain genome stability. Nat. Rev. Mol. Cell Biol. *18*, 315–330.

Desai, S.D., Zhang, H., Rodriguez-Bauman, A., Yang, J.M., Wu, X., Gounder, M.K., Rubin, E.H., and Liu, L.F. (2003). Transcription-dependent degradation of topoisomerase I-DNA covalent complexes. Mol. Cell. Biol. *23*, 2341–2350.

Drolet, M., Broccoli, S., Rallu, F., Hraiky, C., Fortin, C., Massé, E., and Baaklini, I. (2003). The problem of hypernegative supercoiling and R-loop formation in transcription. Front. Biosci. *8*, d210–d221.

Dumitrache, L.C., and McKinnon, P.J. (2017). Polynucleotide kinase-phosphatase (PNKP) mutations and neurologic disease. Mech. Ageing Dev. *161* (Pt A), 121–129.

El Hage, A., French, S.L., Beyer, A.L., and Tollervey, D. (2010). Loss of topoisomerase I leads to R-loop-mediated transcriptional blocks during ribosomal RNA synthesis. Genes Dev. *24*, 1546–1558.

El-Khamisy, S.F., Saifi, G.M., Weinfeld, M., Johansson, F., Helleday, T., Lupski, J.R., and Caldecott, K.W. (2005). Defective DNA single-strand break repair in spinocerebellar ataxia with axonal neuropathy-1. Nature *434*, 108–113.

Graf, M., Bonetti, D., Lockhart, A., Serhal, K., Kellner, V., Maicher, A., Jolivet, P., Teixeira, M.T., and Luke, B. (2017). Telomere length determines TERRA and R-loop regulation through the cell cycle. Cell *170*, 72–85.e14.

Groh, M., and Gromak, N. (2014). Out of balance: R-loops in human disease. PLoS Genet. *10*, e1004630.

Groh, M., Lufino, M.M., Wade-Martins, R., and Gromak, N. (2014). R-loops associated with triplet repeat expansions promote gene silencing in Friedreich ataxia and fragile X syndrome. PLoS Genet. *10*, e1004318.

Groh, M., Albulescu, L.O., Cristini, A., and Gromak, N. (2017). Senataxin: genome guardian at the interface of transcription and neurodegeneration. J. Mol. Biol. *429*, 3181–3195.

Hendrickson, E.A. (1997). Cell-cycle regulation of mammalian DNA double-strand-break repair. Am. J. Hum. Genet. *61*, 795–800.

Hoch, N.C., Hanzlikova, H., Rulten, S.L., Tétreault, M., Komulainen, E., Ju, L., Hornyak, P., Zeng, Z., Gittens, W., Rey, S.A., et al.; Care4Rare Canada Consortium (2017). XRCC1 mutation is associated with PARP1 hyperactivation and cerebellar ataxia. Nature *541*, 87–91.

Huang, S.Y., Ghosh, S., and Pommier, Y. (2015). Topoisomerase I alone is sufficient to produce short DNA deletions and can also reverse nicks at ribonucleotide sites. J. Biol. Chem. *290*, 14068–14076.

Huang, S.N., Williams, J.S., Arana, M.E., Kunkel, T.A., and Pommier, Y. (2017). Topoisomerase I-mediated cleavage at unrepaired ribonucleotides generates DNA double-strand breaks. EMBO J. *36*, 361–373.

Huertas, P., and Aguilera, A. (2003). Cotranscriptionally formed DNA:RNA hybrids mediate transcription elongation impairment and transcription-associated recombination. Mol. Cell *12*, 711–721.

Interthal, H., Chen, H.J., Kehl-Fie, T.E., Zotzmann, J., Leppard, J.B., and Champoux, J.J. (2005). SCAN1 mutant Tdp1 accumulates the enzyme–DNA intermediate and causes camptothecin hypersensitivity. EMBO J. *24*, 2224–2233.

Jeanblanc, M., Ragu, S., Gey, C., Contrepois, K., Courbeyrette, R., Thuret, J.Y., and Mann, C. (2012). Parallel pathways in RAF-induced senescence and conditions for its reversion. Oncogene *31*, 3072–3085.

Jiang, B., Glover, J.N., and Weinfeld, M. (2017). Neurological disorders associated with DNA strand-break processing enzymes. Mech. Ageing Dev. *161* (Pt A), 130–140.

Kannan, A., Bhatia, K., Branzei, D., and Gangwani, L. (2018). Combined deficiency of Senataxin and DNA-PKcs causes DNA damage accumulation and neurodegeneration in spinal muscular atrophy. Nucleic Acids Res. *46*, 8326–8346.

Katyal, S., Lee, Y., Nitiss, K.C., Downing, S.M., Li, Y., Shimada, M., Zhao, J., Russell, H.R., Petrini, J.H., Nitiss, J.L., and McKinnon, P.J. (2014). Aberrant topoisomerase-1 DNA lesions are pathogenic in neurodegenerative genome instability syndromes. Nat. Neurosci. *17*, 813–821.

Kawale, A.S., Akopiants, K., Valerie, K., Ruis, B., Hendrickson, E.A., Huang, S.N., Pommier, Y., and Povirk, L.F. (2018). TDP1 suppresses mis-joining of radiomimetic DNA double-strand breaks and cooperates with Artemis to promote optimal nonhomologous end joining. Nucleic Acids Res. *46*, 8926–8939.

Kim, N., Huang, S.N., Williams, J.S., Li, Y.C., Clark, A.B., Cho, J.E., Kunkel, T.A., Pommier, Y., and Jinks-Robertson, S. (2011). Mutagenic processing of ribonucleotides in DNA by yeast topoisomerase I. Science *332*, 1561–1564.

Li, X., and Manley, J.L. (2005). Inactivation of the SR protein splicing factor ASF/SF2 results in genomic instability. Cell *122*, 365–378.

Löbrich, M., Shibata, A., Beucher, A., Fisher, A., Ensminger, M., Goodarzi, A.A., Barton, O., and Jeggo, P.A. (2010). gammaH2AX foci analysis for monitoring DNA double-strand break repair: strengths, limitations and optimization. Cell Cycle *9*, 662–669.

Ma, L., Cao, X., Wang, H., Lu, K., Wang, Y., Tu, C., Dai, Y., Meng, Y., Li, Y., Yu, P., et al. (2019). Discovery of myricetin as a potent inhibitor of human flap endonuclease 1, which potentially can be used as sensitizing agent against HT-29 human colon cancer cells. J. Agric. Food Chem. *67*, 1656–1665.

Mailand, N., Bekker-Jensen, S., Faustrup, H., Melander, F., Bartek, J., Lukas, C., and Lukas, J. (2007). RNF8 ubiquitylates histones at DNA double-strand breaks and promotes assembly of repair proteins. Cell *131*, 887–900.

Mamouni, K., Cristini, A., Guirouilh-Barbat, J., Monferran, S., Lemarié, A., Faye, J.C., Lopez, B.S., Favre, G., and Sordet, O. (2014). RhoB promotes γH2AX dephosphorylation and DNA double-strand break repair. Mol. Cell. Biol. *34*, 3144–3155.

Manzo, S.G., Hartono, S.R., Sanz, L.A., Marinello, J., De Biasi, S., Cossarizza, A., Capranico, G., and Chedin, F. (2018). DNA topoisomerase I differentially modulates R-loops across the human genome. Genome Biol. *19*, 100.

Marinello, J., Chillemi, G., Bueno, S., Manzo, S.G., and Capranico, G. (2013). Antisense transcripts enhanced by camptothecin at divergent CpG-island promoters associated with bursts of topoisomerase I-DNA cleavage complex and R-loop formation. Nucleic Acids Res. *41*, 10110–10123.

Marinello, J., Bertoncini, S., Aloisi, I., Cristini, A., Malagoli Tagliazucchi, G., Forcato, M., Sordet, O., and Capranico, G. (2016). Dynamic effects of

topoisomerase I inhibition on R-loops and short transcripts at active promoters. PLoS ONE 11, e0147053.

McKinnon, P.J. (2017). Genome integrity and disease prevention in the nervous system. Genes Dev. 31, 1180–1194.

Menon, V., and Povirk, L.F. (2016). End-processing nucleases and phosphodiesterases: An elite supporting cast for the non-homologous end joining pathway of DNA double-strand break repair. DNA Repair (Amst.) 43, 57–68.

Miao, Z.H., Agama, K., Sordet, O., Povirk, L., Kohn, K.W., and Pommier, Y. (2006). Hereditary ataxia SCAN1 cells are defective for the repair of transcription-dependent topoisomerase I cleavage complexes. DNA Repair (Amst.) 5, 1489–1494.

Nitiss, J., and Wang, J.C. (1988). DNA topoisomerase-targeting antitumor drugs can be studied in yeast. Proc. Natl. Acad. Sci. USA 85, 7501–7505.

Nojima, T., Tellier, M., Foxwell, J., Ribeiro de Almeida, C., Tan-Wong, S.M., Dhir, S., Dujardin, G., Dhir, A., Murphy, S., and Proudfoot, N.J. (2018). Deregulated expression of mammalian lncRNA through loss of SPT6 induces R-loop formation, replication stress, and cellular senescence. Mol. Cell 72, 970–984.e7.

Phillips, D.D., Garboczi, D.N., Singh, K., Hu, Z., Leppla, S.H., and Leysath, C.E. (2013). The sub-nanomolar binding of DNA-RNA hybrids by the single-chain Fv fragment of antibody S9.6. J. Mol. Recognit. 26, 376–381.

Pommier, Y. (2006). Topoisomerase I inhibitors: camptothecins and beyond. Nat. Rev. Cancer 6, 789–802.

Pommier, Y., Huang, S.Y., Gao, R., Das, B.B., Murai, J., and Marchand, C. (2014). Tyrosyl-DNA-phosphodiesterases (TDP1 and TDP2). DNA Repair (Amst.) 19, 114–129.

Pommier, Y., Sun, Y., Huang, S.N., and Nitiss, J.L. (2016). Roles of eukaryotic topoisomerases in transcription, replication and genomic stability. Nat. Rev. Mol. Cell Biol. 17, 703–721.

Powell, W.T., Coulson, R.L., Gonzales, M.L., Crary, F.K., Wong, S.S., Adams, S., Ach, R.A., Tsang, P., Yamada, N.A., Yasui, D.H., et al. (2013). R-loop formation at Snord116 mediates topotecan inhibition of Ube3a-antisense and allele-specific chromatin decondensation. Proc. Natl. Acad. Sci. USA 110, 13938–13943.

Ran, F.A., Hsu, P.D., Lin, C.Y., Gootenberg, J.S., Konermann, S., Trevino, A.E., Scott, D.A., Inoue, A., Matoba, S., Zhang, Y., and Zhang, F. (2013). Double nicking by RNA-guided CRISPR Cas9 for enhanced genome editing specificity. Cell 154, 1380–1389.

Rass, U., Ahel, I., and West, S.C. (2007). Defective DNA repair and neurodegenerative disease. Cell 130, 991–1004.

Regairaz, M., Zhang, Y.W., Fu, H., Agama, K.K., Tata, N., Agrawal, S., Aladjem, M.I., and Pommier, Y. (2011). Mus81-mediated DNA cleavage resolves replication forks stalled by topoisomerase I-DNA complexes. J. Cell Biol. 195, 739–749.

Santos-Pereira, J.M., and Aguilera, A. (2015). R loops: new modulators of genome dynamics and function. Nat. Rev. Genet. 16, 583–597.

Sanz, L.A., Hartono, S.R., Lim, Y.W., Steyaert, S., Rajpurkar, A., Ginno, P.A., Xu, X., and Chédin, F. (2016). Prevalent, dynamic, and conserved R-loop structures associate with specific epigenomic signatures in mammals. Mol. Cell 63, 167–178.

Savitsky, K., Bar-Shira, A., Gilad, S., Rotman, G., Ziv, Y., Vanagaite, L., Tagle, D.A., Smith, S., Uziel, T., Sfez, S., et al. (1995). A single ataxia telangiectasia gene with a product similar to PI-3 kinase. Science 268, 1749–1753.

Skourti-Stathaki, K., and Proudfoot, N.J. (2014). A double-edged sword: R loops as threats to genome integrity and powerful regulators of gene expression. Genes Dev. 28, 1384–1396.

Skourti-Stathaki, K., Proudfoot, N.J., and Gromak, N. (2011). Human senataxin resolves RNA/DNA hybrids formed at transcriptional pause sites to promote Xrn2-dependent termination. Mol. Cell 42, 794–805.

Solier, S., Ryan, M.C., Martin, S.E., Varma, S., Kohn, K.W., Liu, H., Zeeberg, B.R., and Pommier, Y. (2013). Transcription poisoning by topoisomerase I is controlled by gene length, splice sites, and miR-142-3p. Cancer Res. 73, 4830–4839.

Sollier, J., and Cimprich, K.A. (2015). Breaking bad: R-loops and genome integrity. Trends Cell Biol. 25, 514–522.

Sollier, J., Stork, C.T., García-Rubio, M.L., Paulsen, R.D., Aguilera, A., and Cimprich, K.A. (2014). Transcription-coupled nucleotide excision repair factors promote R-loop-induced genome instability. Mol. Cell 56, 777–785.

Sordet, O., Larochelle, S., Nicolas, E., Stevens, E.V., Zhang, C., Shokat, K.M., Fisher, R.P., and Pommier, Y. (2008). Hyperphosphorylation of RNA polymerase II in response to topoisomerase I cleavage complexes and its association with transcription- and BRCA1-dependent degradation of topoisomerase I. J. Mol. Biol. 381, 540–549.

Sordet, O., Redon, C.E., Guirouilh-Barbat, J., Smith, S., Solier, S., Douarre, C., Conti, C., Nakamura, A.J., Das, B.B., Nicolas, E., et al. (2009). Ataxia telangiectasia mutated activation by transcription- and topoisomerase I-induced DNA double-strand breaks. EMBO Rep. 10, 887–893.

Sparks, J.L., and Burgers, P.M. (2015). Error-free and mutagenic processing of topoisomerase 1-provoked damage at genomic ribonucleotides. EMBO J. 34, 1259–1269.

Staresincic, L., Fagbemi, A.F., Enzlin, J.H., Gourdin, A.M., Wijgers, N., Dunand-Sauthier, I., Giglia-Mari, G., Clarkson, S.G., Vermeulen, W., and Schärer, O.D. (2009). Coordination of dual incision and repair synthesis in human nucleotide excision repair. EMBO J. 28, 1111–1120.

Takashima, H., Boerkoel, C.F., John, J., Saifi, G.M., Salih, M.A., Armstrong, D., Mao, Y., Quiocho, F.A., Roa, B.B., Nakagawa, M., et al. (2002). Mutation of TDP1, encoding a topoisomerase I-dependent DNA damage repair enzyme, in spinocerebellar ataxia with axonal neuropathy. Nat. Genet. 32, 267–272.

Teasley, D.C., Parajuli, S., Nguyen, M., Moore, H.R., Alspach, E., Lock, Y.J., Honaker, Y., Saharia, A., Piwnica-Worms, H., and Stewart, S.A. (2015). Flap endonuclease 1 limits telomere fragility on the leading strand. J. Biol. Chem. 290, 15133–15145.

Tian, M., and Alt, F.W. (2000). Transcription-induced cleavage of immunoglobulin switch regions by nucleotide excision repair nucleases in vitro. J. Biol. Chem. 275, 24163–24172.

Tresini, M., Warmerdam, D.O., Kolovos, P., Snijder, L., Vrouwe, M.G., Demmers, J.A., van IJcken, W.F., Grosveld, F.G., Medema, R.H., Hoeijmakers, J.H., et al. (2015). The core spliceosome as target and effector of non-canonical ATM signalling. Nature 523, 53–58.

Tuduri, S., Crabbé, L., Conti, C., Tourrière, H., Holtgreve-Grez, H., Jauch, A., Pantesco, V., De Vos, J., Thomas, A., Theillet, C., et al. (2009). Topoisomerase I suppresses genomic instability by preventing interference between replication and transcription. Nat. Cell Biol. 11, 1315–1324.

Walker, C., Herranz-Martin, S., Karyka, E., Liao, C., Lewis, K., Elsayed, W., Lukashchuk, V., Chiang, S.C., Ray, S., Mulcahy, P.J., et al. (2017). C9orf72 expansion disrupts ATM-mediated chromosomal break repair. Nat. Neurosci. 20, 1225–1235.

Wu, J., and Liu, L.F. (1997). Processing of topoisomerase I cleavable complexes into DNA damage by transcription. Nucleic Acids Res. 25, 4181–4186.

Yang, S.W., Burgin, A.B., Jr., Huizenga, B.N., Robertson, C.A., Yao, K.C., and Nash, H.A. (1996). A eukaryotic enzyme that can disjoin dead-end covalent complexes between DNA and type I topoisomerases. Proc. Natl. Acad. Sci. USA 93, 11534–11539.

Yasuhara, T., Kato, R., Hagiwara, Y., Shiotani, B., Yamauchi, M., Nakada, S., Shibata, A., and Miyagawa, K. (2018). Human Rad52 promotes XPG-mediated R-loop processing to initiate transcription-associated homologous recombination repair. Cell 175, 558–570.e11.

STAR★METHODS

KEY RESOURCES TABLE

REAGENT or RESOURCE	SOURCE	IDENTIFIER
Antibodies		
p53BP1 (phospho-Ser1778) rabbit polyclonal antibody (used for: IF)	Cell Signaling Technology	Cat# 2675; RRID:AB_490917
Actin mouse monoclonal antibody (clone C4) (used for: WB)	Millipore	Cat# MAB1501; RRID:AB_2223041
ARTEMIS (DCLRE1C) rabbit monoclonal antibody (clone D708V) (used for: WB)	Cell Signaling Technology	Cat# 13381; RRID:AB_2798197
mCherry rabbit polyclonal antibody (used for: WB)	GeneTex	Cat# GTX128509
CtIP (RBBP8) rabbit polyclonal antibody (used for: WB)	Bethyl	Cat# A300-488A; RRID:AB_2175262
FEN1 rabbit polyclonal antibody (used for: WB)	Bethyl	Cat# A300-255A; RRID:AB_185550
H2AX rabbit polyclonal antibody (used for: ChIP)	Millipore	Cat# 07-627; RRID:AB_2233033
γH2AX (phospho-Ser139) mouse monoclonal antibody (clone JBW301) (used for: IF)	Millipore	Cat# 05-636; RRID:AB_309864
γH2AX (phospho-Ser139) rabbit polyclonal antibody (used for: ChIP)	Millipore	Cat# 07-164; RRID:AB_310406
KAP-1 (TRIM28) rabbit polyclonal antibody (used for: WB)	Bethyl	Cat# A300-274A; RRID:AB_185559
Lamin B1 rabbit polyclonal antibody (used for: WB)	Abcam	Cat# ab16048; RRID:AB_443298
DNA ligase 3 (LIG3, DNL3) rabbit polyclonal antibody (used for: WB)	Bethyl	Cat# A301-636A; RRID:AB_1210932
MRE11 rabbit polyclonal antibody (used for: WB)	Bethyl	Cat# A303-998A; RRID:AB_2620347
MUS81 mouse monoclonal antibody (clone MTA30 2G10/3 (used for: WB)	Abcam	Cat# ab14387; RRID:AB_301167
PNKP (PNK1) rabbit polyclonal antibody (used for: WB)	Bethyl	Cat# A300-257A; RRID:AB_263356
S9.6 mouse monoclonal antibody (used for: DRIP, Slot-blot)	Gromak Lab	N/A; RRID:AB_2810829
ssDNA (single stranded DNA) mouse monoclonal antibody (clone 16-19) (used for: Slot-blot)	Millipore	Cat# MAB3034; RRID:AB_94645
SETX (Senataxin) rabbit polyclonal antibody (used for: WB)	Bethyl	Cat# A301-104A; RRID:AB_873128
SETX (Senataxin) rabbit polyclonal antibody (used for: ChIP)	Novus	NB100-57542; RRID:AB_922411
TDP1 mouse polyclonal antibody (used for: WB)	Abnova Corporation	Cat# H00055775-A01; RRID:AB_461513
αTubulin mouse monoclonal antibody (clone B-5-1-2) (used for: WB)	Sigma-Aldrich	Cat# T5168; RRID:AB_477579
XPF (ERCC4) rabbit polyclonal antibody (used for: WB)	Bethyl	Cat# A301-315A; RRID:AB_938089
XPF (ERCC4) rabbit polyclonal antibody (used for: ChIP and WB)	Abcam	Cat# ab76948; RRID:AB_1524575; Lot#GR172751
XPG (ERCC5) rabbit polyclonal antibody (used for: WB)	Bethyl	Cat# A301-484A; RRID:AB_999684
XRCC1 rabbit polyclonal antibody (used for: WB)	Bethyl	Cat# A300-065A; RRID:AB_2218477
Donkey anti-mouse secondary antibody, Alexa Fluor 488 (used for: IF)	ThermoFisher Scientific	Cat# A-21202; RRID:AB_141607
Goat anti-rabbit secondary antibody, Alexa Fluor 594 (used for: IF)	ThermoFisher Scientific	Cat# A-11037; RRID:AB_2534095
Goat anti-mouse secondary antibody, Alexa Fluor 594 (used for: IF)	ThermoFisher Scientific	Cat# A-11032; RRID:AB_2534091
Goat anti-rabbit secondary antibody, Alexa Fluor 647 (used for: IF)	ThermoFisher Scientific	Cat# A-21245; RRID:AB_2535813
Chemicals, Peptides, and Recombinant Proteins		
Bortezomib (PS-341)	Selleckchem	Cat# S1013; CAS: 179324-69-7
CPT [(S)-(+)-Camptothecin]	Sigma-Aldrich	Cat# C9911; CAS: 7689-03-4

(*Continued on next page*)

Continued

REAGENT or RESOURCE	SOURCE	IDENTIFIER
Dharmafect 4 transfection reagent	Dharmacon	Cat# T-2004
Doxycycline hyclate	Sigma-Aldrich	Cat# D9891; CAS 24390-14-5
FLV (Flavopiridol hydrochloride hydrate)	Sigma-Aldrich	Cat# F3055
Halt Protease & Phosphatase Inhibitor Cocktail	ThermoFisher Scientific	Cat# 1861281
MG132 (Z-Leu-Leu-Leu-al)	Sigma-Aldrich	Cat# C9911; CAS: 133407-82-6
Myricetin	Sigma-Aldrich	Cat# M6760; CAS: 529-44-2
Poly-L-lysine solution	Sigma-Aldrich	Cat# P4832
Proteinase K	Sigma-Aldrich	Cat# 03115828001
RNase H	NEB	Cat# M0297
Critical Commercial Assays		
CellTiter-Blue cell viability assay	Promega	Cat# G8080
Click-iT EdU Alexa Fluor 647 Imaging Kit	ThermoFisher Scientific	Cat# C10340
Click-iT RNA Alexa Fluor 488 Imaging Kit	ThermoFisher Scientific	Cat# C10329
CometAssay Kit	Trevigen	Cat# 4250-050-K
Experimental Models: Cell Lines		
Human: WI38 hTERT cells	Carl Mann laboratory (Jeanblanc et al., 2012)	N/A
Human: XP2Y0 (XPF-deficient) cells	Orlando Schärer laboratory (Staresincic et al., 2009)	N/A
Human: XP2Y0 + XPF WT cells	Orlando Schärer laboratory (Staresincic et al., 2009)	N/A
Human: XP2Y0 + XPF-D676A (nuclease-dead) cells	Orlando Schärer laboratory (Staresincic et al., 2009)	N/A
Human: HCT116 cells	Yves Pommier laboratory (Al Abo et al., 2017)	N/A
Human: HCT116 TDP1 KO cells	Yves Pommier laboratory (Al Abo et al., 2017)	N/A
Human: U2OS cells inducible for mCherry	Patrick Calsou laboratory (Britton et al., 2014)	N/A
Human: U2OS cells inducible for mCherry-RNH1	Patrick Calsou laboratory (Britton et al., 2014)	N/A
Oligonucleotides		
AQR (Aquarius) (human) individual siRNA	Dharmacon	Cat# D-022214-03
ARTEMIS (DCLRE1C) (human) SMARTpool siRNA	Dharmacon	Cat# M-004269-02
CtIP (RBBP8) (human) SMARTpool siRNA	Dharmacon	Cat# M-011376-00
DNA ligase 3 (LIG3, DNL3) (human) SMARTpool siRNA	Dharmacon	Cat# M-009227-02
FEN1 (human) SMARTpool siRNA	Dharmacon	Cat# M-010344-01
LUC (Luciferase GL3 Duplex) siRNA	Dharmacon	Cat# D-001400-01
MRE11 (human) SMARTpool siRNA	Dharmacon	Cat# M-009271-01
MUS81 (human) SMARTpool siRNA	Dharmacon	Cat# L-016143-01
PNKP (human) SMARTpool siRNA	Dharmacon	Cat# M-006783-02
RAD52 (human) SMARTpool siRNA	Dharmacon	Cat# M-011760-01
SETX (Senataxin) (human) siRNA: 5′-UUGGAGUAGUU GAUACCCGAAdTdT-3′	This paper	N/A
TDP1 (human) SMARTpool siRNA	Dharmacon	Cat# M-016112-01
XPF (ERCC4) (human) SMARTpool siRNA	Dharmacon	Cat# M-019946-00
XPG (ERCC5) (human) SMARTpool siRNA	Dharmacon	Cat# M-006626-01
XRCC1 (human) SMARTpool siRNA	Dharmacon	Cat# M-009394-01
Nontargeting control siRNA	Eurogentec	Cat# SR-CL000-005

Continued

REAGENT or RESOURCE	SOURCE	IDENTIFIER
ssDNA: CGGTGTGAATCAGAC (used for DNA/RNA hybrid competition)	Sigma-Aldrich	N/A
ssRNA: GUCUGAUUCACACCG (used for DNA/RNA hybrid competition)	Dharmacon	N/A
See Table S1 for primers used in this study.		
Software and Algorithms		
Columbus software (versions 2.5.0 and 2.8.2)	PerkinElmer	N/A
GraphPad Prism 6.0	GraphPad Prism	https://www.graphpad.com/; RRID:SCR_002798
Harmony software (versions 4.1 and 4.8)	PerkinElmer	N/A
ImageJ software (versions 1.48, 1.51, and 1.52)	National Institutes of Health	https://imagej.nih.gov/ij/; RRID:SCR_003070
OpenComet (version 1.3.1)	OpenComet Software	http://www.cometbio.org
Other		
AxioObserver Z1 fluorescence microscope	ZEISS	https://www.zeiss.com/corporate/int/home.html
LSM 780 confocal microscope	ZEISS	https://www.zeiss.com/corporate/int/home.html
CLARIOstar microplate reader	BMG Labtech	https://www.bmglabtech.com
ChemiDoc MP Imaging System	Bio-Rad	http://www.bio-rad.com
Operetta High-Content Imaging System	PerkinElmer	https://www.perkinelmer.com
Operetta CLS High-Content Imaging System	PerkinElmer	https://www.perkinelmer.com
CellCarrier 96-well	PerkinElmer	Cat# 6005550
Lab-Tek RS chamber slides	ThermoFisher Scientific	Cat# 154526K

LEAD CONTACT AND MATERIALS AVAILABILITY

Further information and requests for resources and reagents should be directed to and will be fulfilled by the Lead Contact, Olivier Sordet (olivier.sordet@inserm.fr). This study did not generate new unique reagents.

EXPERIMENTAL MODEL AND SUBJECT DETAILS

Cells and Treatments

Primary human lung embryonic WI38 fibroblasts (from a 3-month-gestation aborted female fetus) immortalized with hTERT were obtained from Carl Mann (CEA, Gif-sur-Yvette, France) (Jeanblanc et al., 2012). Cells were cultured at 37°C in modified Eagle's medium (MEM) supplemented with 10% (v/v) fetal bovine serum, 1 mM sodium pyruvate, 2 mM glutamine and 0.1 mM non-essential amino acids. To induce quiescence, cells were washed twice with serum-free medium and cultured for 72 h in medium supplemented as described above but with 0.2% (v/v) serum. To control the induction of quiescence in Figures S1A and S1B, cells were incubated with 10 μM EdU for 30 min and the incorporated EdU into DNA was detected using the Click-iT EdU Alexa Fluor 647 imaging kit (ThermoFisher Scientific) according to the manufacturer's protocol. SV40-transformed human fibroblasts XP2Y0 (XPF-deficient, GM08437, from a 64-year-old female), XP2Y0 + XPF WT, and XP2Y0 + XPF-D676A were gifts from Orlando Schärer (Stony Brook University, NY, USA) (Staresincic et al., 2009) and cultured at 37°C in Dulbecco's Modified Eagle's Medium (DMEM) high glucose supplemented with 1 mM sodium pyruvate and 10% (v/v) fetal bovine serum. Human colon carcinoma HCT116 cells (from an adult male) parental and TDP1 KO (Al Abo et al., 2017) and human osteosarcoma U2OS cells (from a 15-year-old female) inducible for mCherry or mCherry-RNH1 (Britton et al., 2014) were cultured at 37°C in DMEM supplemented with 10% (v/v) fetal bovine serum. To express mCherry or mCherry-RNase H1, U2OS cells were treated with 2 μg/ml doxycycline for 24 h. Drugs and chemicals used for treatments are CPT, FLV, MG132, myricetin and doxycycline from Sigma-Aldrich, and bortezomib from Selleckchem. All these agents were dissolved in DMSO except for doxycycline, which was in water. In all the experiments, mock samples were treated with the vehicle only.

METHOD DETAILS

Immunofluorescence Microscopy

Cells were seeded in poly-L-lysine (Sigma-Aldrich)-coated 96-well plates (CellCarrier; PerkinElmer). After treatment, cells were washed twice with PBS and fixed with 3.7% paraformaldehyde for 15 min. After two washes with PBS, cells were permeabilized with 0.5% Triton X-100 for 15 min and washed twice with PBS. Cells were incubated with 8% bovine serum albumin (BSA) in PBS for 1 h before incubation with a mouse anti-γH2AX antibody (05-636; Millipore) and/or a rabbit anti-p53BP1 antibody (#2675; Cell Signaling Technology) diluted at 1/500 in 1% BSA in PBS for 2 h. Cells were washes three times with PBS and incubated with the appropriate secondary antibody coupled to Alexa Fluor 488, 594 or 647 (ThermoFisher Scientific) diluted at 1/500 in 1% BSA in PBS for 1 h. After three washes with PBS, nuclei were stained with 1 μg/ml Hoechst 33342 for 15 min, washed twice with PBS and stored at 4°C until analysis. To identify G1 nuclei, cells were incubated with 10 μM EdU for 30 min before treatment with CPT. The incorporated EdU into DNA was detected using the Click-iT EdU Alexa Fluor 647 Imaging Kit (ThermoFisher Scientific) according to the manufacturer's protocol. After the Click-iT reaction, cells were processed for immunolabelling as described above starting at the 8% BSA step.

96-well plates were scanned with a 20X objective using an Operetta High-Content Imaging System or an Operetta CLS High-Content Imaging System (PerkinElmer) with Harmony software (version 4.1 or 4.8). After data acquisition, subsequent analyses were performed with Columbus software (version 2.5.0 or 2.8.2). γH2AX and p53BP1 foci were detected with the "C" method. Variations of the number of foci between independent experiments can be related to experimental variabilities, which include the automatic counting of foci with Columbus software that depends on the ratio between the signal intensity of foci and background noise. To compare independent experiments, the number of γH2AX/p53BP1 foci were normalized in each individual experiment as indicated in the figure legends. For graphical representation of foci distribution, we used box-and-whisker plots with GraphPad Prism 6 software with the following settings: boxes: 25-75 percentile range; whiskers: 10-90 percentile range; horizontal bars: median number of foci; "+": mean number of foci.

In Figures 1A and 5A, cells were seeded in poly-L-lysine-coated Lab-Tek™ RS chamber slides (NalgeNunc), labeled as described above and slides were mounted using Mowiol 4-88 (Millipore) containing 4',6-diamidino-2-phenylindole (DAPI). Slides were visualized with an inverted confocal microscope (LSM 780; ZEISS) with the objective Plan-Apochromat 63x / 1.4 Oil DIC III. In Figure 5A, γH2AX foci were counted with ImageJ (version 1.48v) as described previously (Cristini et al., 2016).

Chromatin Immunoprecipitation (ChIP)

Chromatin immunoprecipitation was performed as described previously (Cristini et al., 2018; Groh et al., 2014). Briefly, cells were crosslinked with 1% formaldehyde at 37°C for 15 min and the reaction was stopped by adding 0.125 M glycine for 5 min. Pelleted cells were first subjected to lysis with cell lysis buffer (5 mM PIPES pH 8.0, 85 mM KCl, 0.5% NP-40 supplemented with 0.5 mM PMSF and 1X Complete EDTA-free protease inhibitors, Sigma-Aldrich) to isolate nuclei. Pelleted nuclei were then incubated in nuclear lysis buffer (50 mM Tris-HCl pH 8.0, 5 mM EDTA, 1% SDS supplemented with 0.5 mM PMSF and 1X Complete EDTA-free protease inhibitors, Sigma-Aldrich) and sonicated (Diagenode Bioruptor). After removal of insoluble material by centrifugation, samples were diluted with ChIP IP buffer (16.7 mM Tris-HCl pH 8.0, 1.2 mM EDTA pH 8.0, 167 mM NaCl, 0.01% SDS, 1.1% Triton X-100 supplemented with 0.5 mM PMSF and 1X Complete EDTA-free protease inhibitors, Sigma-Aldrich) and precleared by adding protein A agarose beads (16-157; Millipore). Chromatin was then incubated overnight at 4°C with anti-γH2AX (07-164; Millipore), anti-H2AX (07-627; Millipore), anti-SETX (NB100-57542; Novus Biologicals), anti-XPF (ab76948; Abcam Lot#GR172751) antibodies or no antibody. Immunocomplexes were retrieved by incubation with protein A agarose beads (16-157; Millipore). Beads were then washed once with buffer A (20 mM Tris-HCl pH 8.0, 2 mM EDTA, 0.1% SDS, 1% Triton X-100 and 0.15 M NaCl), once with buffer B (20 mM Tris-HCl pH 8.0, 2 mM EDTA, 0.1% SDS, 1% Triton X-100 and 0.5 M NaCl), once with buffer C (10 mM Tris-HCl pH 8.0, 1 mM EDTA, 1% NP-40, 1% Sodium Deoxycholate and 0.25 M LiCl) and then twice with buffer D (10 mM Tris-HCl pH 8.0 and 1 mM EDTA). Beads were eluted in 1% SDS and 0.1 M NaHCO3 and samples decross-linked by addition of RNase A and NaCl (0.3 M) at 65°C for at least 4 h. After 2 h proteinase K (Sigma-Aldrich) digestion at 45°C, DNA was purified with QIAquick PCR purification kit (QIAGEN), and analyzed by qPCR with Rotor-Gene® Q (QIAGEN). The amount of immunoprecipitated material at a particular gene region was calculated as the percentage of input after subtracting the background signal (no antibody control). Unless otherwise stated, data were normalized to the DMSO-treated sample in each experiment, which was set equal to 1. The primers used for ChIP are listed in Table S1.

RNA/DNA Immunoprecipitation (DRIP)

RNA/DNA immunoprecipitation was carried out as described in (Cristini et al., 2018; Skourti-Stathaki et al., 2011) with the S9.6 antibody (Boguslawski et al., 1986). Briefly, isolated non-crosslinked nuclei were subjected to nuclear lysis (50 mM Tris-HCl pH 8.0, 5 mM EDTA, 1% SDS) and digestion with Proteinase K (Sigma-Aldrich) for 3 h at 55°C. Genomic DNA was precipitated, resuspended in IP dilution buffer (16.7 mM Tris-HCl pH 8.0, 1.2 mM EDTA, 167 mM NaCl, 0.01% SDS, 1.1% Triton X-100) and sonicated (Diagenode Bioruptor) to obtain DNA fragments of about 500 bp. Sonicated genomic DNA was then precleared with protein A agarose beads (16-157; Millipore) in presence of protease inhibitors (0.5 mM PMSF, 0.8 μg/ml pepstatin A, 1 μg/ml leupeptin). 10 μg of genomic DNA were incubated overnight at 4°C with 15 μl of S9.6 antibody or no antibody control. Addition of beads, washes, and elution steps

were carried out following the same procedure described for ChIP. RNase H sensitivity was performed by adding 1.7 U RNase H (M0297; NEB) per microgram of genomic DNA for 2.5 h at 37°C before IP step. The amount of immunoprecipitated material at a particular gene region was calculated as the percentage of input after subtracting the background signal (no antibody control). Unless otherwise stated, data were normalized to the β-actin TSS proximal probe of the DMSO-treated sample in each experiment, which was set equal to 1. The primers used for DRIP are listed in Table S1.

RNA/DNA Hybrid Slot Blot

Slot blot experiments were carried out as described (Cristini et al., 2018) using the S9.6 antibody (Boguslawski et al., 1986). Genomic DNA preparation and RNase H digestion were performed following the procedure described for DRIP. For loading control, 350 ng of genomic DNA were heated at 95°C for 10 min, loaded on the slot blot and the membrane was denatured for 10 min in 0.5 M NaOH, 1.5 M NaCl, and neutralized for 2 min in 0.5 M Tris-HCl pH 7.2, 1.5 M NaCl. The membrane was probed with an anti-ssDNA antibody (MAB3034; Millipore) after UV crosslinking and saturating. Images were acquired with LAS-4000 (Fujifilm). S9.6 and ssDNA signals were quantified using Image Studio Lite software (Li-COR Biosciences).

RNA/DNA Hybrid Co-immunoprecipitation

RNA/DNA hybrid co-IP was performed as described (Cristini et al., 2018) using the S9.6 antibody (Boguslawski et al., 1986). Briefly, non-crosslinked nuclei were incubated in RSB buffer (10 mM Tris-HCl pH 7.5, 200 mM NaCl, 2.5 mM MgCl2) with 0.2% sodium de-oxycholate, 0.1% SDS, 0.05% sodium lauroyl sarcosinate and 0.5% Triton X-100, and sonicated for 10 min (Diagenode Bioruptor). Samples were then diluted 4 times in RSB with 0.5% Triton X-100 (RSB + T) before IP with the S9.6 antibody, bound to protein A dynabeads (Invitrogen), and preblocked with 0.5% BSA/PBS for 2 h. IP was performed in presence of 0.1 ng of RNase A (PureLink, Invitrogen) per microgram of genomic DNA. Beads were then washed 4 times with RSB + T and 2 times with RSB. IPs were eluted in 1x LDS (Invitrogen), 100 mM DTT for 10 min at 70°C for SDS-PAGE, and in 1% SDS and 0.1 M NaHCO3 for 30 min at room temperature for RNA/DNA hybrid slot blot. Where indicated, RNA/DNA hybrid competitors were added during the IP step at 1.3 μM concentration (Phillips et al., 2013). RNA/DNA hybrids were prepared as described in (Cristini et al., 2018; Phillips et al., 2013) (ssDNA- CGGTGTGAATCAGAC; ssRNA-GUCUGAUUCACACCG). RNA/DNA hybrid IP with RNase H treatment was carried out as described previously (Cristini et al., 2018). Proteins were separated on 4%–12% Bis-Tris or 3%–8% Tris-Acetate gels by SDS-PAGE (Invitrogen) and immunoblotted with anti-XPF (ab76948; Abcam Lot#GR172751) and anti-lamin B1 (ab16048; Abcam) antibodies. XPF signal was quantified by using ImageJ (version 1.52h). XPF IP signal was normalized to XPF input signal and the DMSO-treated sample was set to 1.

Cell Extracts and Immunoblotting

Cell extracts were obtained by lysing cells for 15 min at 4°C in buffer containing 50 mM Tris-HCl (pH 8.0), 300 mM NaCl, 0.4% NP-40, 10 mM MgCl2 and 5 mM DTT, supplemented with protease and phosphatase inhibitors (Halt Protease & Phosphatase Inhibitor Cocktail; ThermoFisher Scientific). After centrifugation (10,000 x g, 20 min), supernatants were diluted (v/v) in 50 mM Tris-HCl (pH 8.0), 0.4% NP-40 and 5 mM DTT. Proteins were separated by SDS-PAGE and immunoblotted with the following antibodies at dilutions recommended by the manufacturer: anti-pan-actin (MAB1501; Millipore), anti-ARTEMIS (#13381; Cell Signaling Technology), anti-mCherry (GTX128509; GeneTex), anti-CtIP (A300-488A; Bethyl), anti-FEN1 (A300-255A; Bethyl), anti-KAP1 (A300-274A; Bethyl), anti-DNA ligase3 (A301-636A; Bethyl), anti-MRE11 (A303-998A; Bethyl), anti-MUS81 (ab14387; Abcam), anti-PNKP (A300-257A; Bethyl), anti-SETX (A301-104A; Bethyl), anti-TDP1 (H00055775-A01; Abnova Corporation), anti-αtubulin (T5168; Sigma-Aldrich), anti-XPF (A301-315A; Bethyl), anti-XPG (A301-484A; Bethyl), and anti-XRCC1 (A300-065A; Bethyl). Immunoblotting was revealed by chemiluminescence using a ChemiDoc MP Imaging System (Bio-Rad).

Comet Assays

Neutral and alkaline comet assays were performed according to the manufacturer's instructions (Trevigen), except that electrophoresis was performed at 4°C. Slides were scanned by using a AxioObserver Z1 fluorescence microscope (ZEISS) with the objective EC Plan-Neofluar 10X / 0.3 Ph1. Comet tail moments were measured with ImageJ software (version 1.51n) with the plugin OpenComet (http://www.cometbio.org).

siRNA Transfection

Cells were transfected with siRNA duplexes using Dharmafect 4 transfection reagent (Dharmacon) for 24 h before inducing quiescence for 72 h. siRNAs used are pools of 4 siRNAs per gene from Dharmacon [CtIP: M-011376-00-0005; ARTEMIS (DCLRE1C): M-004269-02; DNA ligase 3: M-009227-02; FEN1: M-010344-01; MRE11: M-009271-01; MUS81: L-016143-01; PNKP: M-006783-02; RAD52: M-011760-01; TDP1: M-016112-01; XPF: M-019946-00; XPG: M-006626-01; XRCC1: M-009394-01], or are individual siRNAs from Eurofins Genomics (SETX: 5′-UUGGAGUAGUUGAUACCCGAAdTdT-3′), Dharmacon (AQR: D-022214-03; LUC control sequence: D-001400-01), or Eurogentec (nontargeting control sequence: SR-CL000-005).

Quantification of Global RNA Transcription

Global RNA transcription was detected in cells using the Click-iT RNA Alexa Fluor 488 Imaging Kit (ThermoFisher Scientific). Cells were seeded in poly-L-lysine-coated Lab-Tek^{TM} RS chamber slides (NalgeNunc) and incubated with 1 mM EU for 30 min to label newly synthesized RNA, which was detected according to the manufacturer's instructions. Slides were mounted using Mowiol 4-88 (Millipore) containing PI and scanned by using an AxioObserver Z1 fluorescence microscope (ZEISS) with the objective Plan-Apochromat 20X / 0.8. Pictures were analyzed with ImageJ (version 1.48v).

Cell Viability Assays

CellTiter-Blue cell viability assays were performed into 96-well microplates (CellCarrier; PerkinElmer) according to the manufacturer's instructions (Promega) and fluorescence was measured at 545-20 nm Ex/600-40 nm Em using a CLARIOstar microplate reader (BMG Labtech). Viability of untreated cells was set to 100%.

QUANTIFICATION AND STATISTICAL ANALYSIS

Information on biological replicates (n) is indicated in the figure legends. For immunofluorescence microscopy experiments, at least 500 nuclei were analyzed when using the Operetta/Columbus system and at least 150 nuclei when using counting with ImageJ in Figure 5A. For comet assays, at least 150 nuclei were analyzed. Experimental differences were tested for significance with one-way ANOVA or two-tailed unpaired t test by using GraphPad Prism 6 software. Ns indicates not significant differences. $p < 0.05$ is considered significant. $*p < 0.05$, $**p < 0.01$, $***p < 0.001$, $****p < 0.0001$.

DATA AND CODE AVAILABILITY

This study did not generate/analyze datasets/code.